

**Experimental Study of the Frequency Correlation  
of Space-Time Entangled Photons**

by

Eric A. Dauler

Submitted to the Department of Electrical Engineering and Computer Science  
in Partial Fulfillment of the Requirements for the Degrees of

Bachelor of Science in Electrical Engineering and Computer Science  
and Master of Engineering in Electrical Engineering and Computer Science

at the Massachusetts Institute of Technology

June 2003

Copyright 2003 Eric A. Dauler. All rights reserved.

The author hereby grants to M.I.T. permission to reproduce and  
distribute publicly paper and electronic copies of this thesis  
and to grant others the right to do so.

Author \_\_\_\_\_  
Department of Electrical Engineering and Computer Science  
May 20, 2003

Certified by \_\_\_\_\_  
Steven Constantine  
Lincoln Laboratory Thesis Supervisor

Certified by \_\_\_\_\_  
Franco N. C. Wong  
M.I.T. Thesis Supervisor

Accepted by \_\_\_\_\_  
Arthur C. Smith  
Chairman, Department Committee on Graduate Theses

# **Experimental Study of the Frequency Correlation of Space-Time Entangled Photons**

by

Eric A. Dauler

Submitted to the  
Department of Electrical Engineering and Computer Science

June 2003

In Partial Fulfillment of the Requirements for the Degree of  
Bachelor of Science in Electrical Engineering and Computer Science  
and Master of Engineering in Electrical Engineering and Computer Science

## **ABSTRACT**

Space-time entangled photons generated from a continuous-wave parametric downconverter have a well defined sum-frequency despite having individual broad bandwidths. The narrowband frequency correlation that results from this well defined sum-frequency is examined experimentally. The measurements use degenerate, 1.55  $\mu\text{m}$  photon pairs that are also suitable for fiber-based quantum communication protocols. Techniques for optimizing the pair generation rate, the detector and coincidence circuit parameters and the fiber coupling of downconverted light are also presented. A strong frequency correlation is observed using  $\sim 0.5$  nm bandpass filters to measure the frequencies of entangled photons with  $>100$  nm individual bandwidths.

Thesis Supervisor: Franco N. C. Wong

Title: Senior Research Scientist, Research Laboratory of Electronics

## ACKNOWLEDGEMENTS

First, I would like to thank the three people I consider my advisors. I have always been amazed by how Franco Wong, my on-campus thesis advisor, could find my experimental mistakes and send me in the right direction without the benefit of actually seeing the experimental setup. His weekly suggestions were instrumental in my understanding and completing this work. Secondly, Steven Constantine has served as my Lincoln Laboratory advisor, teaching me important lessons about cleaning and aligning the Ti:Sapphire laser and other optics. His assistance in obtaining funding along with finding the equipment to speed along data collection has been greatly appreciated. I am also grateful for his daily stories and distractions, which helped make my hours in the dark lab far more enjoyable. Finally, Marius Albot, a colleague, graciously offered his expertise and advice while also serving as a link between Lincoln Laboratory and MIT campus. This thesis would not have been possible without his work on designing and building the photon counters.

I would also like to thank the many other people who helped me complete this work. Professor Jeffrey Shapiro provided the theoretical background which inspired this work and helped me understand the mathematics behind it. William Keicher supported this research as the Optical Communications Technology Group Leader, providing additional funding as well as a new laboratory. Peg Danek, Tim Yarnall, Dave Caplan, Scott Hamilton, and Shelby Savage provided additional guidance and help with equipment at Lincoln Laboratory.

I would not have worked on the thesis at all without the help of several people. I owe my initial interest in this area to enthusiasm and patient guidance of my first advisor, Dr. Alan Migdall at NIST. His guidance several years ago provided me with the foundation and insights that allowed me to design and perform these experiments. Most importantly, however, my parents provided the support and encouragement to keep me involved in research from high school through my undergraduate education at MIT. Their sacrifices have given me the opportunity to pursue all of my goals.

Finally, I would like to thank my girlfriend, Sandi Lin, for her encouragement, patience, and support. Her concurrent thesis work was a model of what can be accomplished with motivation and focus, helping drive me to finish this work. But it is her support, which helped me through the inevitable mistakes, for which I am truly indebted to her.

# TABLE OF CONTENTS

<b>CHAPTER 1 - INTRODUCTION .....</b>	<b>7</b>
1.1 Correlated and Entangled Photon Pairs .....	7
1.2 Proposed Experiment .....	7
1.3 Parametric Fluorescence .....	10
1.4 Single Photon Detection .....	11
<b>CHAPTER 2 - DETECTION AND GENERATION OF SINGLE PHOTON PAIRS .....</b>	<b>13</b>
2.1 Single Photon Detection at 1.55 $\mu\text{m}$ .....	13
2.2 Coincident Detection at 1.55 $\mu\text{m}$ .....	17
2.3 Quasi-phasematching in Periodically Poled Lithium Niobate.....	21
<b>CHAPTER 3 - EXPERIMENTAL DESIGN.....</b>	<b>24</b>
3.1 Experimental Arrangement.....	24
3.2 Crystal Temperature Optimization .....	36
3.3 Pair Generation Rate Optimization.....	39
<b>CHAPTER 4 - EXPERIMENTAL RESULTS.....</b>	<b>43</b>
4.1 Bulk and Waveguide Crystal Comparison.....	43
4.2 Frequency Correlation Demonstration.....	46
4.3 Detected Light Statistics .....	48
<b>CHAPTER 5 - CONCLUSION .....</b>	<b>54</b>
5.1 Technical Achievements.....	54
5.2 Concluding Remarks.....	54
<b>REFERENCES.....</b>	<b>57</b>

# LIST OF FIGURES

Figure 1-1: Proposed Experimental Setup .....	9
Figure 2-1: Count rate as a function of time within the gate interval for detector 1 (left) and detector 2 (right) .....	16
Figure 2-2: 18-ns-long average detection efficiency as a function of wavelength (-50°C; 4-V, 20-ns-long gates) .....	17
Figure 2-3: Coincidence rate as a function of the time difference between paired detections .....	18
Figure 2-4: Histogram of coincidence rate as a function of the time difference between detector gating pulse. The line shows the convolution of the detector efficiencies in time. ....	19
Figure 2-5: Quasi-phasematched wavelengths as a function of temperature with poling period = 18.984 $\mu\text{m}$ .....	22
Figure 3-1: Free-space portion of the experimental setup .....	29
Figure 3-2: Fiber portion of the experimental setup .....	32
Figure 3-3: Equivalence between a (a) 50/50 splitter and a (b) frequency splitter with 3dB insertion loss .....	33
Figure 3-4: Schematic of the experimental setup for the conversion efficiency measurement ....	37
Figure 3-5: Conversion efficiency per nm of output bandwidth as a function of crystal temperature and fluorescence wavelength .....	38
Figure 3-6: Conversion efficiency per nm of output bandwidth at crystal temp = 34°C .....	39
Figure 4-1: Theoretical (lines) and experimental (shapes) coincidence signal to noise ratio for bulk and waveguide crystals .....	45
Figure 4-2: (a) Transmission curve for grating demultiplexer channel 5; (b) Counts over 300 second period for single detector (open triangles) and coincidences (filled squares) as a function of tunable filter wavelength .....	47
Figure 4-3: (a) Transmission curve for grating demultiplexer channels 5-8; (b) Normalized coincidence rate as a function of tunable filter wavelength .....	48
Figure 4-4: Transmission curve for channels 4 and 5 of the grating demultiplexer .....	53

## LIST OF TABLES

Table 3-1: Beam parameters for three focusing arrangements considered experimentally.....	27
Table 3-2: Insertion loss of components at 1550 nm.....	35
Table 4-1: Ratio of coincidences to singles with corrections listed in left column.....	51
Table 4-2: Ratio of coincidences to singles with corrections listed in left column.....	53

# CHAPTER 1 - INTRODUCTION

## 1.1 *Correlated and Entangled Photon Pairs*

Entanglement was first considered as an argument against quantum mechanics, when Einstein, Podolsky, and Rosen argued that the states of particles must be pre-determined if simultaneous, non-local measurements lead to correlated results [1]. The question of non-locality remained untested until Bell reposed the problem in terms of experimentally testable inequalities [2]. Experimental evidence has since argued against the existence of hidden variables [3], finding instead that the state of entanglement remains undetermined until a measurement is made. Although measurement of one particle instantaneously determines the state of both particles, entanglement does not allow information to be transmitted faster than the speed of light because information about the result still must be sent classically from one location to the other. Entangled particles do, however, provide many possibilities for applications that are not allowed classically. Entangled photons, for example, have been used for experiments ranging from quantum metrological techniques [4] to demonstrations of the power of quantum information [5].

Polarization entanglement is a well-studied example of entangled photons. One case of polarization-entangled photons is described by the wavefunction:

$$|\Psi\rangle = |h_1\rangle|v_2\rangle + |v_1\rangle|h_2\rangle, \quad (1-1)$$

where the subscripts 1 and 2 are labels for the two photons and "h" and "v" represent orthogonal polarization states. Regardless of how far photons 1 and 2 are separated, the measurement of one photon's polarization instantaneously determines the polarization of the other photon, although neither polarization was fixed before the measurement. This uniquely quantum behavior, the second particle being projected into the conjugate state, is what gives entangled particles the ability to do things that classical systems cannot.

## 1.2 *Proposed Experiment*

Although entanglement in polarization, which has only two orthogonal states, has been well studied [6], entanglement of continuous variables such as frequency, has attracted much less experimental attention. The proposed research in this thesis examines the frequency

characteristics of parametrically downconverted photon pairs and relates them to the polarization entanglement described above. Specifically, a detector is placed after a narrowband filter and the detection of one photon from a pair is shown to determine the frequency of the conjugate photon of the same pair.

Therefore, the goal of this work is to demonstrate the quantum magic bullet effect, which is presented in reference [7]. The term “quantum magic bullet” is used to describe the property of continuous-variable entangled particles in which the passage of one particle through a scattering potential is accompanied by the passage of the second particle through a related potential. This phenomenon is the result of a measurement of the first particle projecting the second particle into the complex conjugate, or time-reversed, state. The quantum magic bullet effect for frequency-entangled photons explains how the passage of one photon through a narrowband filter forces the paired photon to penetrate the conjugate filter with unity probability.

Although it may seem that there is a simple, classical explanation for this “magic bullet” phenomenon, namely the conservation of energy, it is important to note that the individual photons need to have well-defined frequencies in this classical interpretation. The filter penetration effect could be obtained using a non-entangled mix of frequency-correlated photons only if the individual photons have narrowband frequencies. This is analogous to using predefined sets of orthogonally polarized photons in the polarization measurement described in section 1.1.

These non-entangled states, however, can be clearly distinguished from entangled states. This distinction has been well studied for both polarization, in terms of Bell measurements [8], and frequency, using Hong-Ou-Mandel quantum interference experiments [9]. Hong-Ou-Mandel interference measurements can be used to demonstrate that individual photons produced in parametric downconversion have broad bandwidths. Given these broad bandwidths, it is not possible to explain the filter penetration phenomenon classically. This uniquely quantum behavior, where an individually broadband photon is projected into a narrowband spectrum, is the quantum magic bullet effect.

The applications of frequency entanglement have not been fully explored, but many potential possibilities exist within the field of quantum communication. Classical optical communication is often done through fibers at wavelengths near 1.55  $\mu\text{m}$ . Although single photon detectors for this wavelength are still experimental, this wavelength was chosen because

of potential practical applications and the wide availability of spectral filtering components. Additionally, optical fibers provide a good environment for making single photon measurements because stray light outside the fiber is blocked to a large extent.

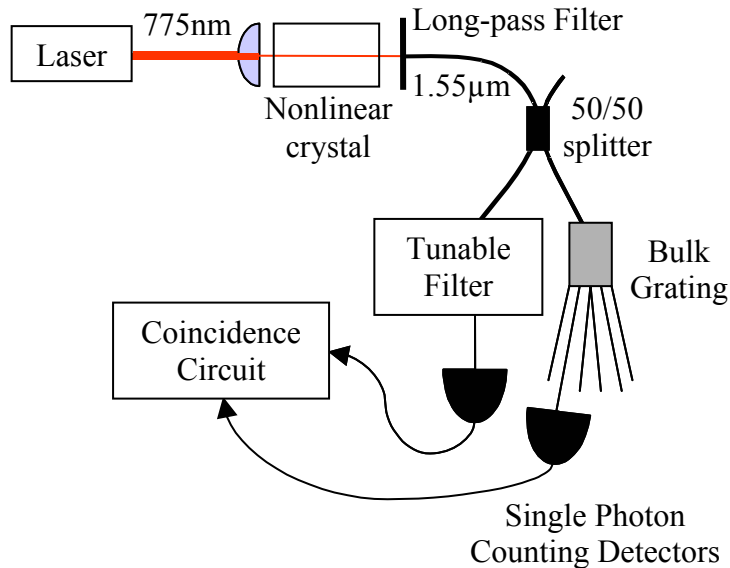


**Figure 1-1: Proposed Experimental Setup**

In a typical setup, such as in Figure 1-1, pairs of frequency correlated photons are produced using an intense pump beam in a nonlinear crystal via parametric fluorescence, which is described in section 1.3. The intense pump beam is blocked after the crystal with a long-pass filter and the paired photons are coupled into a single-mode fiber. Once in the fiber, the photons are sent through a 50/50 fiber coupler so that half of the time the two photons from a pair are split into different output fibers. One output fiber is connected to a tunable filter that removes light at all frequencies except for a narrow range. The frequency bandwidth of the tunable filter is much smaller than the spectral bandwidth of the down-converted photons, so the filter projects the indeterminate frequency of the broadband photons into a much narrower, well-defined frequency range.

The other output fiber is connected to a grating filter with eight non-overlapping, narrowband channels. This grating filter is a common telecommunications component for frequency multiplexing and de-multiplexing. In this setup, the tunable filter in the first path

performs a frequency measurement on one photon that projects the conjugate photon into a frequency that is determined by the energy conservation relation (see section 1.3). The energy conservation requirement is enforced even when the projective measurements are made after the two photons are well separated. This is clearly indicative of a quantum-mechanical, rather than classical, effect.

Fiber-coupled photon counting detectors are placed after each filtering component to measure the photons' arrival times. The detector outputs are sent to a coincidence circuit consisting of a time to amplitude converter (TAC) and single channel analyzer (SCA), which only generate an output pulse if both detectors fire simultaneously. An electronic counter is used to record both the number of coincidences and the number of counts from each detector.

When the tunable filter is set to the frequency conjugate to the grating filter channel, both photons from the pair can reach the detectors and coincidence counts occurs within the narrow time window defined by the SCA. If the tunable filter is offset from the conjugate frequency, both photons from a pair do not reach the detectors and coincidence counts are the result of noise alone. The frequency projection can therefore be observed by measuring the number of coincidences as the frequency of the tunable filter is adjusted.

### **1.3 Parametric Fluorescence**

The most common and convenient source of entangled photons is spontaneous parametric downconversion, which is also called parametric fluorescence. Parametric fluorescence is a three wave mixing process in which intense light from a laser interacts with a nonlinear medium to produce pairs of lower energy photons. These photons are frequency entangled as a result of the conservation of energy:

$$\omega_p = \omega_s + \omega_i, \tag{1-2}$$

where  $\omega$  is the frequency of each photon, the subscripts s and i are labels for the entangled photons (referred to as signal and idler) and the subscript p labels the photon from the intense pump beam. For each pair of signal and idler photons generated, a pump photon is destroyed in the process.

Efficient downconversion occurs only for frequencies and propagation directions where both energy and momentum are conserved. The momentum of a photon is related to the index of

refraction of the surrounding medium. Since the index of materials is frequency dependent, momentum conservation, or phasematching, can rarely be achieved for collinear waves within a particular nonlinear crystal. With only a limited number of crystals available, one of two techniques is often used to obtain phasematching for a particular set of frequencies.

A birefringent crystal can be used because the indices of refraction are both frequency and directionally dependent, which allows phasematching to occur for a wide range of frequencies along different output directions. Unfortunately, the cones of down-converted light generated by this technique are difficult to collect efficiently, especially into single-mode fibers.

A second technique uses the periodic inversion of the nonlinear coefficient as the additional degree of freedom to allow user-selected frequencies to be phase-matched. Periodically poled lithium niobate (PPLN) is one example of a material whose nonlinear coefficient can be inverted by applying a large electric field. The distance between periodically inverted regions then determines the frequencies of the down-converted photons. Additionally, a waveguide can be built into the crystal so that light is produced in a single spatial mode. This has the advantage that all of the downconverted light can be coupled into a single-mode fiber.

## **1.4 Single Photon Detection**

The drawback to working with photons at  $1.55\ \mu\text{m}$  is the difficulty of single photon counting at that wavelength. Although photo-multiplier tubes (PMTs) and single photon counting silicon (Si) avalanche photodiodes (APDs) are commercially available for visible wavelengths, the options for single photon detection at  $1.55\ \mu\text{m}$  are very limited. The best choice is to use a biasing and gating circuit to operate commercially available InGaAs APDs in Geiger mode, which allows the absorption of a single photon to generate an avalanche of electrons.

After an avalanche, the flow of electrons must be stopped before a second detection is possible. Although Si single photon counting APDs are often actively quenched, allowing photons to be counted at rates up to  $\sim 10\ \text{MHz}$ , InGaAs single photon counting detectors are usually passively quenched. The circuit must gate the detector above the breakdown voltage for a set amount of time, regardless of whether a photon is detected. After this relatively short time period, the voltage is brought down below breakdown and the detector is given a long recovery

period before again being biased above breakdown. The detector performs best at rates of  $\sim 50$  kHz or less [10].

Unfortunately, in addition to a slower detection rate, cooled InGaAs single photon detectors have greater than  $10^4$  dark counts per second and quantum efficiencies around 15%. This is far worse than the 100 dark counts per second and 70% efficiencies that can be expected for single photon counting APDs at visible frequencies. The challenge is therefore to keep the loss in the system as low as possible, so that the dark counts do not overwhelm the down-converted photons and an acceptable signal to noise ratio can be achieved.

# CHAPTER 2 - DETECTION AND GENERATION OF SINGLE PHOTON PAIRS

## 2.1 *Single Photon Detection at 1.55 $\mu\text{m}$*

Although the detection of photons at 1.55  $\mu\text{m}$  is not the focus of this work, an understanding of the detection process is necessary to minimize the noise that is introduced to the measurement. As mentioned in the introduction, the best detectors available for single photon counting at 1.55  $\mu\text{m}$  are InGaAs APDs operated in Geiger mode. While this technology has recently become commercially available, it has also been the subject of study at MIT [10]. The commercially available photon counters have similar performance as those built at MIT, but do not allow as many operating parameters to be optimized for coincident detection. The tradeoffs in adjusting the operating parameters and the detector performance are discussed in this section.

InGaAs APDs designed for linear-mode operation are commercially available from several manufacturers. The APDs best suited for Geiger-mode operation are manufactured by JDS Uniphase [10], although a considerable variation in performance between photodiodes has been found. A circuit for quenching the flow of electrons and for outputting a pulse following a detection event must be built to operate an APD in Geiger mode.

A passive quenching circuit is one in which the detector is gated into Geiger mode for only short time intervals. The length of the gate is independent of whether an avalanche event occurs, so the amount of current that flows through the APD following a photon detection event is proportional to the length of the gating pulse. This amount of current is important because it affects the number of electrons that become trapped in the APD. Following each gating pulse, the APD must be biased at a voltage below breakdown for a long period, allowing time for all of the trapped electrons to exit the APD. If this time period is not long enough, an afterpulse can occur when a trapped electron triggers an avalanche during the next gating interval. Afterpulses must be considered separately from dark counts because afterpulses tend to occur at the beginning of a gate interval rather than having Poisson distributed arrival times. If afterpulses are not suppressed, they are more likely to generate noise in the coincidence rate than dark counts.

Several operating parameters can be easily changed to optimize the detectors' performance. First, the temperature of the APD is important because it affects the detection efficiency, the dark count rate and the rate at which electrons flow out of the APD during quenching. We are most concerned with minimizing the dark count rate while maximizing the detection efficiency. Increasing the rate at which electrons flow out of the APD is also desirable, but a long interval between gates can be used to compensate for a slow electron flow rate. The dark counts, detection efficiency and electron flow rate all increase by raising temperature, so it is clear that some compromise is necessary.

In addition to adjusting the temperature, the bias voltage, gate voltage and gate timing must be selected. Increasing the bias voltage increases both the dark counts and the detection efficiency, so there is again some tradeoff. It is important to keep this bias voltage below breakdown. Increasing the gate voltage improves the detection efficiency without significantly changing the dark counts, so the gate voltage was set to the maximum of 4V supplied by the pulse generator. The gain in detection efficiency achieved by increasing the gate voltage from 3V to 4V is small, so it is unlikely that a higher voltage pulse generator can improve the detector performance significantly.

The length of the gate and the time between gates, or duty cycle, must be chosen after considering the focus of the experiment. The measurement of interest for this experiment is the coincidence rate, so it is particularly important to limit noise that results in accidental coincidence detection events. The non-Poissonian character of afterpulses makes them more likely to generate erroneous coincidence counts, so it is very important to limit the afterpulse rate. The afterpulse rate can be reduced by decreasing the current flow (gate length) or increasing the time between gates. Both of these options decrease the duty cycle, so decreasing the afterpulse probability is achieved by lowering the detection duty cycle.

However, other noise sources affecting the coincidence rate must also be considered. Although the noise on a single detector counting rate is proportional to the gate length, the coincidence noise from dark counts is dependent on the coincidence window length. Similarly, the noise from uncorrelated, downconverted pairs is proportional to the coincidence window length. The length of the coincidence window is limited by the detector timing jitter, which is independent of all the adjustable parameters, so the coincidence window should be minimized as far as the timing jitter allows. We can, however, increase the gate length without affecting the

noise on the coincidence rate. Since the rise time of the gating pulse is on the order of 1 ns, we want to select a considerably longer than 1-ns gate interval to minimize the low detection efficiency periods at the beginning and end of the gate. The gate length is limited in practice because we do not want the single detector counts rates to be overwhelmed by the dark counts.

Some explicit data on these relationships can be found in work that is focused on the detection process [10] while other parameters were set based on the practical limitations mentioned above. The operating parameters were optimized for coincidence detection and all data taken using these settings for consistency. The detectors were operated at  $-50^{\circ}\text{C}$  with 4-V, 20-ns-long gates at a 40 kHz repetition rate (0.08% duty cycle). The bias voltage was device dependent and was selected to give similar dark count rates for the two detectors; it was usually set at approximately 0.5-V below the breakdown voltage.

Given that the experiments focus on measuring frequency correlation, it is important that we measure the detection efficiency as a function of wavelength. Additionally, any variations with time may also be important given that we are concerned with coincidence measurements. The detection efficiency measurements were performed using an HP 8168A tunable laser operated at  $100\ \mu\text{W}$ , well within its operating range of  $10\ \mu\text{W}$  to  $1\ \text{mW}$ . An HP 86120B Multi-Wavelength Meter was used to verify that the laser wavelength was accurate to  $\sim 10\ \text{pm}$ . A JDS Uniphase HA9 Variable Attenuator was used along with a 95/5 splitter to attenuate the laser light. The splitting ratio of the 95/5 splitter was calibrated as a function of wavelength and the 95% channel was connected to a power meter module (HP 81532A) in an HP Lightwave multimeter (HP 8153A). The power meter had a  $-110\ \text{dBm}$  sensitivity and a  $0.1\ \text{pW}$  ( $-100\ \text{dBm}$ ) accuracy. The 5% channel was attenuated to  $\sim 0.5\ \text{pW}$  (0.07 photons per 20 ns gate) and connected to the photon counting APDs.

The resulting detections were counted using a Picoquant TimeHarp 200 computer board that records the difference in the arrival times of two pulses. The output from the detector was connected to the Start channel while a delayed copy of the gating pulse was sent to the Sync channel. A histogram showing the number of counts at each time within a gate was generated. A resolution of 148 ps was used for this histogram with a measurement jitter of  $\sim 150\ \text{ps}$ . The total count rate measured using the Picoquant board matched the rate measured using an Ortec 974 Quad 100 MHz Quad Counter. The Picoquant board's accuracy in measuring the shape of the histogram was verified using an Ortec 567 TAC and SCA.

The histogram shape is expected to match the square shape of the gating pulse, but turns out to be non-uniform for both detectors (Figure 2-1). The shape of the counting rate as a function of time within the gating interval is found to be the same for all wavelengths measured from 1460 nm to 1580 nm. Additionally, the same shape is found for dark counts alone, when there is no input light. Although careful efforts were made to match impedances, the non-uniform shape is most likely the result of reflections within the quenching or bias circuits.

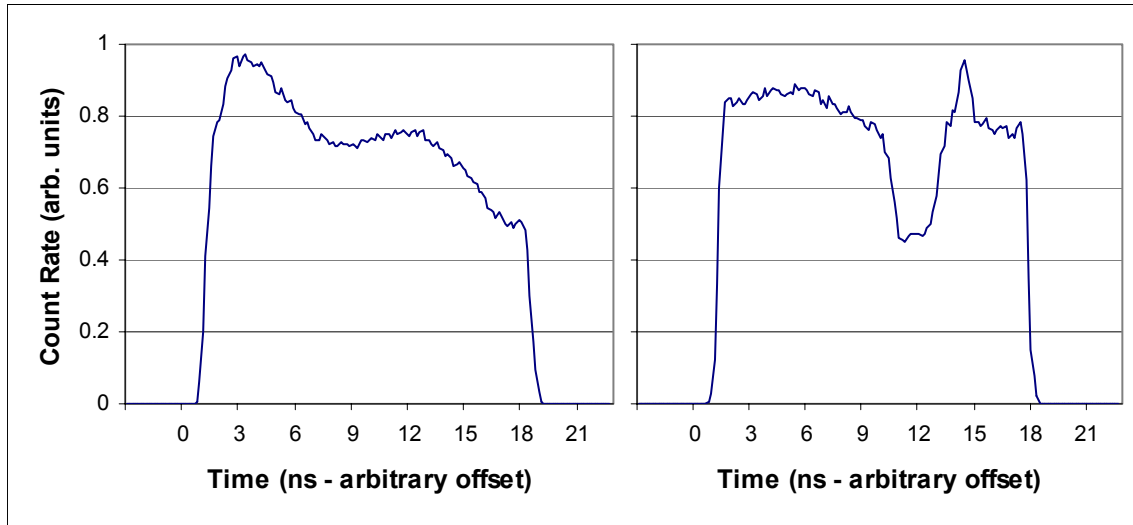


**Figure 2-1: Count rate as a function of time within the gate interval for detector 1 (left) and detector 2 (right)**

The detection probability is calculated using the total count rates, the dark count rate, the splitting ratio, the power measured on the 95% channel, and the photon energy at each measured wavelength. Additionally, the length of the gate interval is needed in order to translate the incident power into a probability per gate. The gate interval is found to be ~18 ns, the full width of the detection histograms. The formula to calculate the 18-ns-long average detection efficiency is:

$$Eff(\lambda) = \frac{[Counts(\lambda) - DarkCounts] \frac{hc}{\lambda}}{Split(\lambda) Power(\lambda) GateLength} , \quad (2-1)$$

where  $\lambda$  is the wavelength,  $Counts(\lambda)$  is the average number of counts per gate,  $DarkCounts$  is the average number of dark counts per gate,  $h$  is Planck's constant,  $c$  is the speed of light,

Split( $\lambda$ ) is the splitting ratio (power in the 5% output over power in the 95% output), Power( $\lambda$ ) is the measured power on the 95% channel, and GateLength = 18 ns. The variables listed as functions of wavelength were measured separately at each wavelength.

The 18-ns average detection efficiencies as a function of wavelength are shown in Figure 2-2. The detection efficiency is shown to decrease slightly as the wavelength increases from 1460 nm to 1550 nm and then decreases more quickly at wavelengths greater than 1550 nm. The 18-ns-long average detection efficiencies for the two detectors at 1550 nm (-50°C; 4-V, 20-ns-long gates) are found to be 17.7% and 13.4%, with dark count rates of  $3.9 \times 10^4/s$  and  $4.4 \times 10^4/s$  respectively.

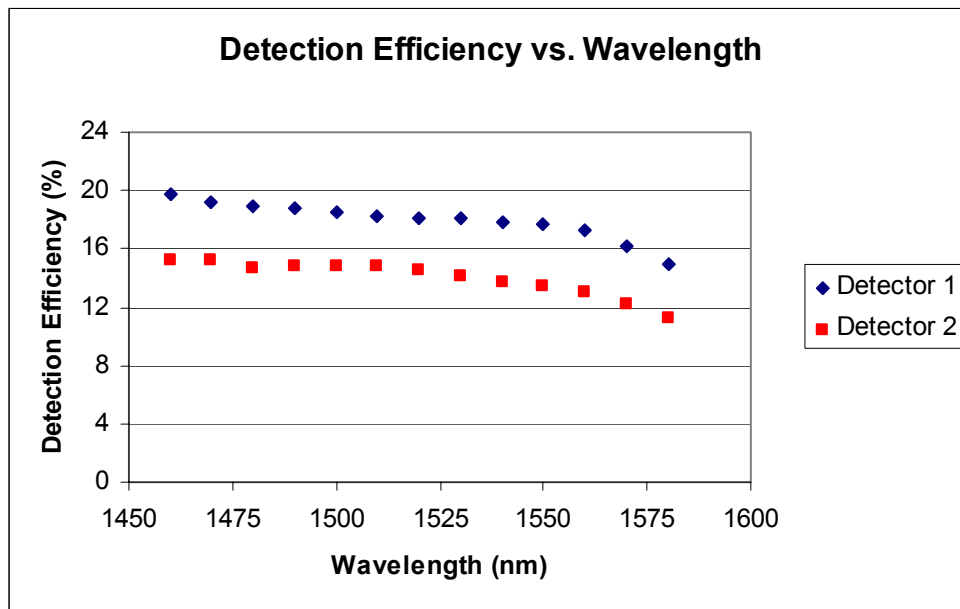
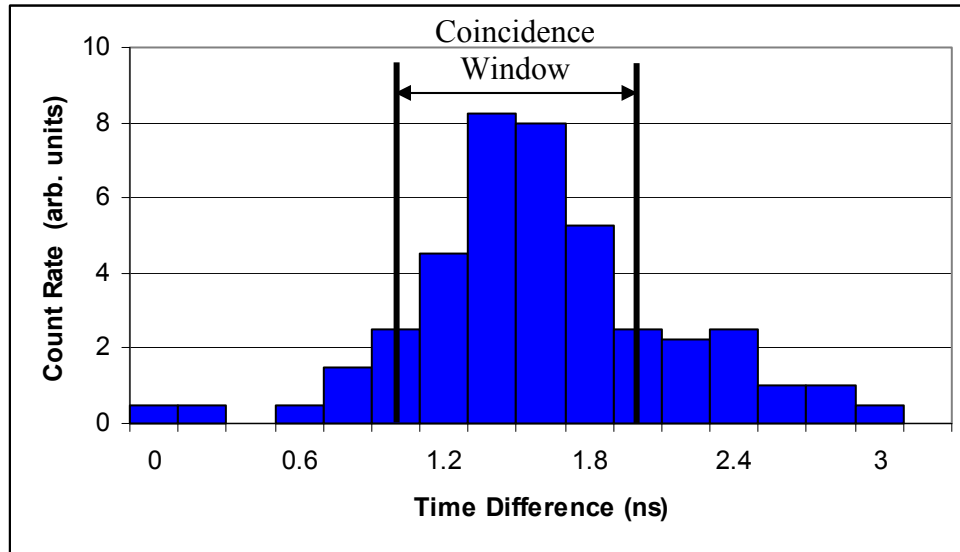


Figure 2-2: 18-ns-long average detection efficiency as a function of wavelength (-50°C; 4-V, 20-ns-long gates)

## 2.2 Coincident Detection at 1.55 $\mu\text{m}$

The experiment proposed in section 1.2 requires that we distinguish paired detection events from single detection events. The Ortec 567, which combines the functions of a TAC and SCA, is used as a coincidence circuit. The output from one detector is connected to the start channel of the TAC and the output from the second detector is delayed using several meters of coaxial cable before it is connected to the stop channel. The coincidence time window,  $\tau_c$ , is the

range of arrival time differences within which the SCA is set to yield a coincidence count. This window is an adjustable parameter of the SCA, and the timing jitter of the detectors and electronics limits the minimum  $\tau_c$  length. The SCA limits the  $\tau_c$  length to be at least 100 ps.



**Figure 2-3: Coincidence rate as a function of the time difference between paired detections**

The total system timing jitter can be measured by setting the SCA to a very narrow time span and producing a histogram of the coincidence rate as a function of  $\tau_c$ . This histogram is flat when there are no timing correlations between detections, but has a sharp peak when most of the detections are the result of paired photons. A histogram where most coincidences are the result of paired detections is shown in Figure 2-3. The tails of this peak do not in fact go to zero because there is the flat background coincidence rate. The background or noise in the coincidence rate is the result of dark counts and uncorrelated photon pairs. It is important to limit the number of background coincidence counts occurring within the coincidence window, so a narrow, 1-ns coincidence window is also shown in Figure 2-3. The importance of this coincidence window in optimizing the experiment is discussed in section 3.3 and a 1-ns window is used in all of the measurements.

Once the coincidence window has been centered on the peak in coincidence rate, we must also optimize the relative time at which the detectors are gated into Geiger mode. The detector gating should be timed to compensate for any fiber length differences, so that both photons arrive at the same point within their respective detectors' gating intervals. The pulse generator has two

separate outputs that provide variable gating pulses for the detectors. The relative timing of these pulses can be digitally adjusted with picosecond resolution, so this timing can be set to compensate for any mismatch in fiber and coaxial lengths between detectors. By adjusting the relative output timing over a broad range, the coincidence rate should be modulated by the convolution of the two detector efficiencies versus gate time shown in Figure 2-3. The resulting coincidence rate is shown in Figure 2-4 along with the calculated convolution of the two detectors' efficiency versus gate time shapes.

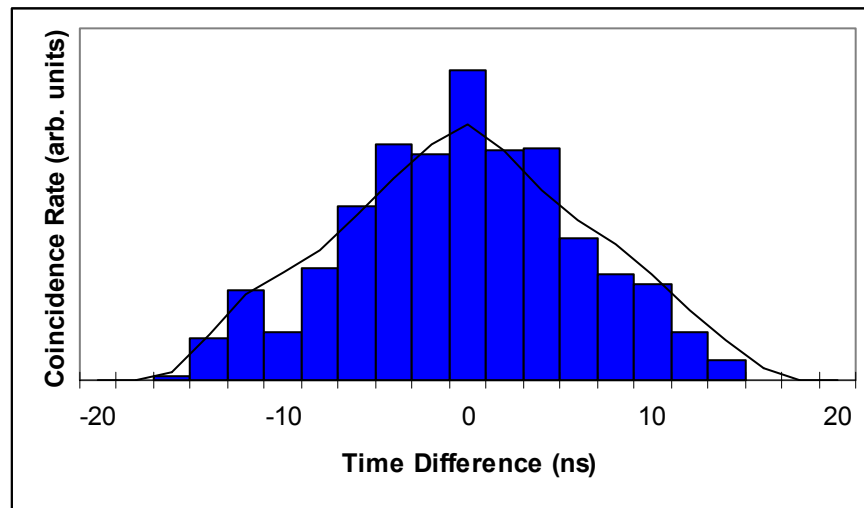


**Figure 2-4: Histogram of coincidence rate as a function of the time difference between detector gating pulse. The line shows the convolution of the detector efficiencies in time.**

The time difference setting on the pulse generator should be set based on the peak of this histogram. Although the coaxial cable lengths are fixed for all experiments, the fiber lengths are changed slightly by connecting different output channels from the diffraction grating. These changes can be accurately measured by finding the peak in coincidence rate as a function of the SCA (coincidence window) position, as shown in Figure 2-3. This measurement can also be used to adjust the time difference setting on the pulse generator, since the coaxial cable lengths remain constant.

Now that the coincidence circuit has been optimized, we may develop a better definition of detection efficiency. Rather than the 18-ns-long average detection efficiency described in section 2.1, the detection efficiency can be conditioned on the fact that the conjugate photon of

the pair is detected. Detection efficiency is used in section 4.3 to account for differences between the single and coincidence counting rates, so this conditional definition of detection efficiency is more appropriate.

The conditional detection efficiency is calculated from the data shown in Figure 2-1. In order to calculate the conditional detection efficiency for detector A, we must first determine its detection efficiency as a function of time (relative to the gate) using equation 2.1 for each of the 148 ps data collection windows. We then multiply detector A's time-dependent efficiency by a probability distribution for registering a count in detector B. This probability distribution represents the condition that, as a function of time relative to the gate, detector B counts a photon. A photon at detector B must be accompanied by a conjugate photon at detector A, so we are really conditioning the efficiency of detector A on the fact that the conjugate photon of the pair is detected. Since we are using a continuous-wave process, detector B's probability distribution is simply its counting rate as a function of time (Figure 2-1) divided by its total counting rate. We integrate this product of detector B's probability distribution and detector A's time-dependent detection efficiency to find the total conditional detection efficiency for detector A.

This conditional detection efficiency is useful for calculating the number of single, trigger counts that are expected to lead to coincidence counts. The measured conditional detection efficiencies are slightly higher than 18-ns-long average detection efficiencies because both detectors tend to have higher efficiency in the first half of the gate. The conditional detection efficiencies at 1550 nm (50°C; 4-V, 20-ns-long gates) are found to be 18.9% and 14.3%, with dark counts of  $3.9 \times 10^4$  and  $4.4 \times 10^4$  per second respectively.

In addition to optimizing the coincidence circuit for counting paired photons, we must experimentally measure the background in the coincidence rate. Background coincidences can occur because of simultaneous dark counts, a dark count and a photon count or two photon counts from different pairs, so blocking the parametric fluorescence does not give an accurate background measurement. The best way to measure the background is to offset both the coincidence window and the gating pulses by an amount large enough to yield zero true coincidences between photon pairs, ~20 ns. The offset in gate timing turns the detectors on at different times, preventing any paired events from being seen by both detectors. It does not, however, affect the single counting rates because the pairs are produced in a continuous-wave

process. The SCA is also offset, so that coincidences occur between events that are 20 ns apart. This correlates events that occur at the same relative time with respect to the start of the gate at each of the two detectors. Since the noise is uncorrelated to begin with, offsetting both the gating pulses and the SCA allows the background to be measured experimentally.

### **2.3 Quasi-phasematching in Periodically Poled Lithium Niobate**

Parametric fluorescence from a nonlinear crystal is used to generate frequency correlated pairs of photons. Since the experiments are performed in single-mode fibers, it is convenient for the paired photons to be produced collinearly so both can be coupled into the same fiber. A collinear configuration is most easily obtained using a periodically-poled material, and PPLN was chosen because of its high nonlinearity and wide availability.

Quasi-phasematching is achieved by periodically inverting the nonlinear coefficient to compensate for the waves' different phase velocities. The required domain reversal period can be calculated from the material's indices of refraction and the desired polarization and frequency of the waves involved in the interaction [11]:

$$\Lambda = \frac{2\pi}{k_p - k_s - k_i}, \quad (2-2)$$

where  $\Lambda$  is the domain reversal period and  $k_p$ ,  $k_s$ ,  $k_i$  are the wave vectors of the pump, signal and idler fields in the crystal, respectively. Choosing all photons to be e-polarized allows the conversion efficiency to be maximized by using the largest nonlinear coefficient in lithium niobate,  $d_{33}$ . The reversal period for a pump wavelength of 775 nm and degenerate outputs at 1550 nm is  $\sim 19 \mu\text{m}$ . This can be achieved by patterning electrodes, using lithographic techniques, and applying a large voltage to the crystal.

The indices of refraction in lithium niobate are temperature dependent, so a small, constant error in the poling period can be corrected by adjusting the crystal temperature. A large adjustment in the crystal temperature allows different sets of wavelengths to be quasi-phasematched, as is shown in Figure 2-5. PPLN is often designed to be operated at high temperatures in order to increase the damage threshold, which is limited at low temperatures by the photo-refractive effect. The powers necessary for this experiment are less than 100 mW, so the crystal poling period was selected for near room temperature operation.

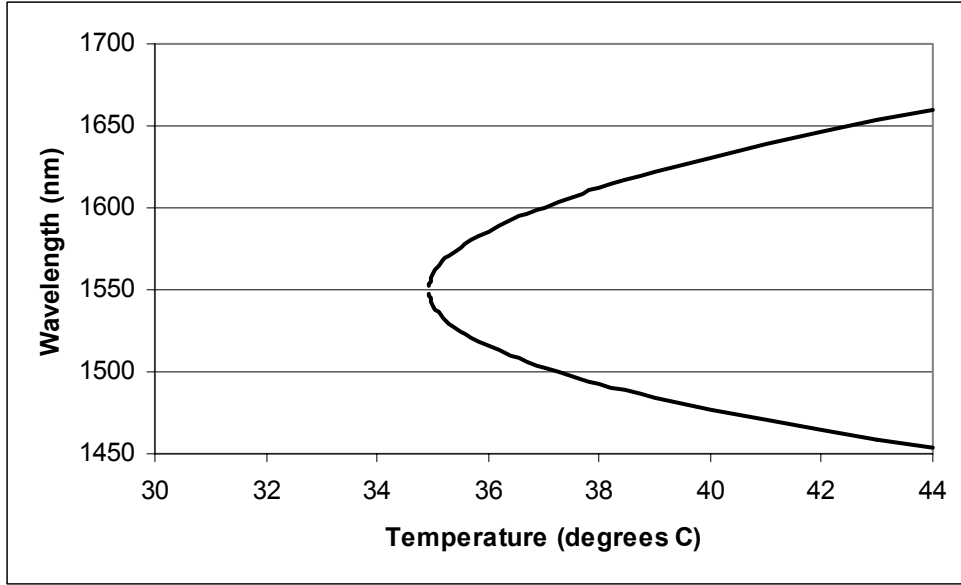


**Figure 2-5: Quasi-phasematched wavelengths as a function of temperature with poling period = 18.984  $\mu\text{m}$**

The spectral bandwidth of the parametric fluorescence process is determined by the length of the PPLN crystal. The relationship between the bandwidth and crystal length can be derived from the efficiency of the downconversion process, which is proportional to the well-known factor [12]:

$$P_s(l) \propto \left( \frac{\sin(\Delta kl/2)}{\Delta kl/2} \right)^2. \quad (2-3)$$

We can see that the spectral bandwidth is wider for shorter crystal lengths. Near degeneracy (where  $\omega_{s0} \approx \omega_{i0}$ ), we can calculate the FWHM of the output bandwidth by expanding the index of refraction as a function of frequency into a second order Taylor series. Assuming the pump has negligible bandwidth and the signal and idler photons are collinearly polarized, the fluorescence bandwidth is:

$$\Delta\omega_s = \Delta\omega_i = 2 \sqrt{\frac{\pi c}{l} \left[ 2 \left. \frac{\partial n_{eff}(\omega)}{\partial \omega} \right|_{\omega_{s0}} + \left. \frac{\partial^2 n_{eff}(\omega)}{\partial \omega^2} \right|_{\omega_{s0}} \right]^{-1}}, \quad (2-4)$$

where  $\omega_{s0}$ ,  $\omega_{i0}$  are the signal and idler center frequencies,  $n_{\text{eff}}$  is the material's index of refraction,  $l$  is the total length of the poled region and  $c$  is the speed of light in vacuum.

The fluorescence bandwidth needs to be considerably wider than the bandwidths of the tunable filter and the demultiplexer because of the projective measurements discussed in the introduction. An eight channel, 200 GHz spacing grating demultiplexer was selected, resulting in a  $\sim 10$  nm range of interest. With  $l = 10$  mm, the calculated FWHM output bandwidth is  $\sim 140$  nm, thus providing a constant output intensity over the region of interest. The output bandwidth has been measured experimentally, as described in section 3.2.

## CHAPTER 3 - EXPERIMENTAL DESIGN

### 3.1 *Experimental Arrangement*

The collinear phasematching conditions that are considered in section 2.3 are an exact solution only if the interacting waves are infinite plane waves. Furthermore, parametric fluorescence involves the interaction of an intense pump beam with quantum fluctuations, so fluorescence is generated in any mode that spatially overlaps the pump, although non-collinear interactions have different phasematching conditions. It is clear, therefore, that we must give particular attention to the collection of downconverted light in single-mode fibers. Coupling downconversion outputs into fibers has been the subject of both experimental [13] and theoretical [14] work, but a simple, optimal solution has not been found. Previous work has focused on non-collinear arrangements that are suitable for collecting the output from a birefringently phasematched crystal. A collinear arrangement was chosen for this experiment in the hope that it would simplify the collection process and allow a direct comparison between bulk and waveguided crystals.

The goal is to design a collection arrangement such that, given that one of the downconverted photons is coupled, the probability of coupling the conjugate photon into the fiber is maximized. It is not important that we couple a high fraction of the total fluorescence output because we may ignore fluorescence output modes that are not coupled into the fiber. There are, however, two additional considerations. First, the PPLN crystal has a finite thickness limited by the difficulty of poling thick crystals. The crystal used in this work was purchased from Deltronic Crystal Industries and is 0.5 mm thick. Furthermore, the heater used to control the temperature of the crystal, purchased from Super Optronics Corp., is designed for crystals up to 2 cm in length, thus limiting the beam diameter to less than 0.5 mm for the entire 2 cm heater length. A second consideration is the desire to maximize the conversion efficiency of the collected mode because the pump power is limited.

Given these restrictions, we have chosen an arrangement similar to the one presented by Kurtsiefer et al. [13]. A lens is positioned so that the fiber's near-Gaussian input mode has a long confocal parameter when imaged back into the crystal. It is important that the confocal parameter be considerably longer than the crystal so that the mode's wavefronts are approximately planar inside the crystal, as assumed in section 2.3 for analyzing the

phasematching conditions. If we consider downconverted photons in the coupled output mode as being generated by signal and idler quantum fluctuations, we would ideally like the pump to be an infinite plane wave so the signal and the conjugate idler spatial modes are degenerate. Unfortunately, the pump must be focused into the crystal to avoid clipping on the edges of the heater and to obtain reasonable conversion efficiency. The Kurtz et al. [13] group obtained both high conversion efficiency and good conditional coupling by matching the pump waist to the waist of the coupled fluorescence mode, so the same choice has been made for this work.

Although a theoretical framework for analyzing these focusing parameters was not available when the experiments were performed, there has been recent work to develop one [14]. This work assumes that the mode coupled into the fiber is a quasi-plane and quasi-monochromatic wave. This assumption is met when we consider a reasonably narrow bandwidth of downconverted light and when the confocal parameter of the coupled mode is much longer than the crystal. Our experimental arrangement also meets the assumption that the coupling lens not act as a limiting aperture. The final assumption is that the output plane of the crystal be imaged onto the tip of the fiber. This is close, but not exactly equivalent to imaging the Gaussian fiber mode to the center of the crystal, as we intend to do. The distance from the lens to the fiber is optimized experimentally, so the actual imaging condition is set to maximize the conditional coupling efficiency. Assuming the crystal output plane is imaged, the expression developed for the conditional coupling efficiency is [14]:

$$\eta = 4 \frac{(1 + \xi^2)}{(2 + \xi^2)^2} \frac{\text{erf}(\sigma_c)}{\sigma_c} \sqrt{\frac{\sigma_1}{\text{erf}(\sigma_1)} \frac{\sigma_2}{\text{erf}(\sigma_2)}}, \quad (3-1)$$

where  $\xi$  is the ratio of the imaged fiber mode diameter to the pump diameter inside the crystal and

$$\sigma_c = \frac{L}{r_p} \sqrt{\frac{(\alpha_1 + \alpha_2)\xi^2 + \beta}{\xi^2(2 + \xi^2)}}; \sigma_j = \frac{L}{r_p} \sqrt{\frac{\alpha_j}{1 + \xi^2}}. \quad (3-2)$$

The parameters  $\alpha_j$  and  $\beta$  are related to the transverse separation of the downconverted photons as they travel through the crystal and  $r_p$  is the pump radius. The transverse separations have contributions from both walkoff and the propagation angle of the downconverted photons. The walkoff is exactly zero for the collinear quasi-phasematched interaction we are considering. The

collected mode is approximately collinear with the pump, so we can solve for the conditional coupling efficiency as the downconverted photon's propagation angle approaches zero. In this limit,  $\sigma_c$ ,  $\sigma_1$ , and  $\sigma_2$  approach zero and the ratio of  $\sigma_i/\text{erf}(\sigma_i)$  approaches one, regardless of the length of the crystal,  $L$ , or the radius of the pump beam,  $r_p$ . For the collinear case, we are left with:

$$\eta = 4 \frac{(1 + \xi^2)}{(2 + \xi^2)^2}. \quad (3-3)$$

As predicted, this conditional coupling efficiency approaches unity as the pump beam diameter is made much wider than the collected downconversion mode diameter ( $\xi \rightarrow 0$ ). In the focusing arrangement we have chosen for the experiments, with equivalent pump and collection mode diameters ( $\xi = 1$ ), this calculation predicts a ~89% conditional coupling efficiency. This coupling efficiency is reasonably high, particularly compared to the other losses in the system, so we can be confident that the selected focusing arrangement is appropriate.

We may now calculate the confocal parameter, beam waist and lens positions using the equations for transforming a Gaussian beam [15]:

$$\text{(Magnification)} \quad M = \frac{\left| \frac{f}{z-f} \right|}{\sqrt{1 + \left( \frac{z_0}{z-f} \right)^2}} \quad (3-4)$$

$$\text{(Waist Location)} \quad (z' - f) = M^2(z - f) \quad (3-5)$$

$$\text{(Beam Waist)} \quad w_0' = Mw_0 \quad (3-6)$$

$$\text{(Confocal parameter)} \quad b' = 2z_0' = 2\pi w_0'^2/\lambda \quad (3-7)$$

$$\text{(Radius of curvature)} \quad R(z) = z \left[ 1 + \left( \frac{z_0}{z} \right)^2 \right], \quad (3-8)$$

where the primed variables denote values after transformation and the unprimed variables are before transformation. The variable  $z$  is the distance between the beam waist and the lens,  $z_0$  is the Rayleigh range, or half the confocal parameter  $b$ ,  $w_0$  is the beam waist (radius),  $f$  is the focal length of the lens, and  $\lambda$  is the wavelength. Wavelength is dependent on the surrounding

medium's index of refraction, so both the waist location and the confocal parameter change inside the crystal. For convenience, however, we calculate the beam parameters using the vacuum wavelength and correct for the non-unity index by considering the crystal's effective length. The  $L = 10$  mm PPLN crystal, with an index of refraction of  $n = 2.2$ , has an effective length of  $L / n = 4.5$  mm.

A Coherent 5W Verdi is used to pump a Coherent 899 Ring Laser configured for Ti:Sapphire operation. The Ti:Sapphire output has a beam waist of 0.3 mm at a distance of 5 cm before the output coupler. Three focusing arrangements were used in this work and their relevant parameters are given in Table 3-1. Since the effective crystal length is shorter than the confocal parameter for all of the arrangements, it is clear that the maximum wavefront curvature occurs at the edges of the crystal. The radius of curvature of the downconverted wavefront is given at the edges of the effectively 4.5 mm long crystal. The lens used for coupling the downconversion into fiber was a Newport F-L10B multi-element lens with a focal length of 12 mm.

<b>Arrangement</b>	<b>#1</b>	<b>#2</b>	<b>#3</b>
Lens Position (z)	2 m	1.2 m	1.5 m
Focal Length (f)	300 mm	300 mm	500 mm
Crystal Position (z')	351 mm	386 mm	721 mm
Pump Beam Free Space Confocal Parameter (b')	21.7 mm	69.6 mm	161 mm
Pump and Downconversion Beam Waist ( $w_0'$ )	51.8 $\mu\text{m}$	92.7 $\mu\text{m}$	141 $\mu\text{m}$
Downconversion Free Space Confocal Parameter	10.9 mm	34.8 mm	80.5 mm
Downconversion Radius of Curvature at $\pm 2.25$ mm	15.4 mm	137 mm	722 mm
Fiber Coupling Lens Position (z'')	131 mm	223 mm	327 mm

**Table 3-1: Beam parameters for three focusing arrangements considered experimentally**

It is clear that the first arrangement does not meet the criteria that the coupled mode be a quasi-plane wave inside the crystal. This wavefront has a 15.4 mm radius of curvature at the edges of the crystal, which is close to the beam's maximum, 10.9 mm, radius of curvature. This arrangement is only used for the measurement of conversion efficiency as a function of wavelength and crystal temperature presented in section 3.2. This arrangement is selected to

maximize the signal to noise ratio for the single detector used to make this measurement. The rest of the experiments presented here use the second or third arrangement, which have much longer confocal parameters. These experiments involve coincidence measurements, so it is not as important that the single detector rates are well above the dark counts.

The problem of selecting the optimal output mode can be eliminated by using a single-mode waveguide, which has only been recently demonstrated for use in entanglement generation [16]. In a waveguide, only a single mode of downconverted light can propagate, so it is only the efficiency with which this mode can be coupled into the fiber that is of concern. Additionally, the pump can be confined over the entire length of the waveguide, so the pump power needed to achieve the same conversion efficiency as a bulk crystal is much lower. The index of refraction inside the waveguide is different from the bulk crystal's index, so the waveguide requires a different poling period from that calculated in section 2.3.

A 1-cm-long PPLN waveguide designed for second-harmonic generation of 1550 nm light was purchased from HC Photonics Corp. Design parameters such as the index change and poling period are not known, but the phasematching conditions and nonlinear coefficient for second-harmonic generation and degenerate parametric downconversion are the same, so this crystal also works for our application.

An experimental arrangement can now be designed for performing the frequency correlation experiments in both the bulk and waveguide crystals as shown in Figure 3-1. The orientation of the bulk crystal and waveguide are each set so that the polarization exiting the polarizing beamsplitter (PBS) is extraordinary inside the crystals. A portion of the beam is split off before it is sent to the waveguide to monitor the wavelength using a HP 86120B Multi-Wavelength Meter and the power using a Coherent Ultima Labmaster with a 33-0944 germanium sensor. The HP 86120B can measure wavelengths down to 700 nm with 10  $\mu$ W sensitivity. The 33-0944 is only designed to measure wavelengths down to 800 nm, but is sensitive to  $\sim 50$  nW of light at 775 nm. The readings from this power meter are used primarily to measure fluctuations in the laser power, while a Coherent FieldMaster-GS with a LM-3 sensor is used to measure the absolute laser power. A scale factor for the 33-0944 readings can therefore be determined.

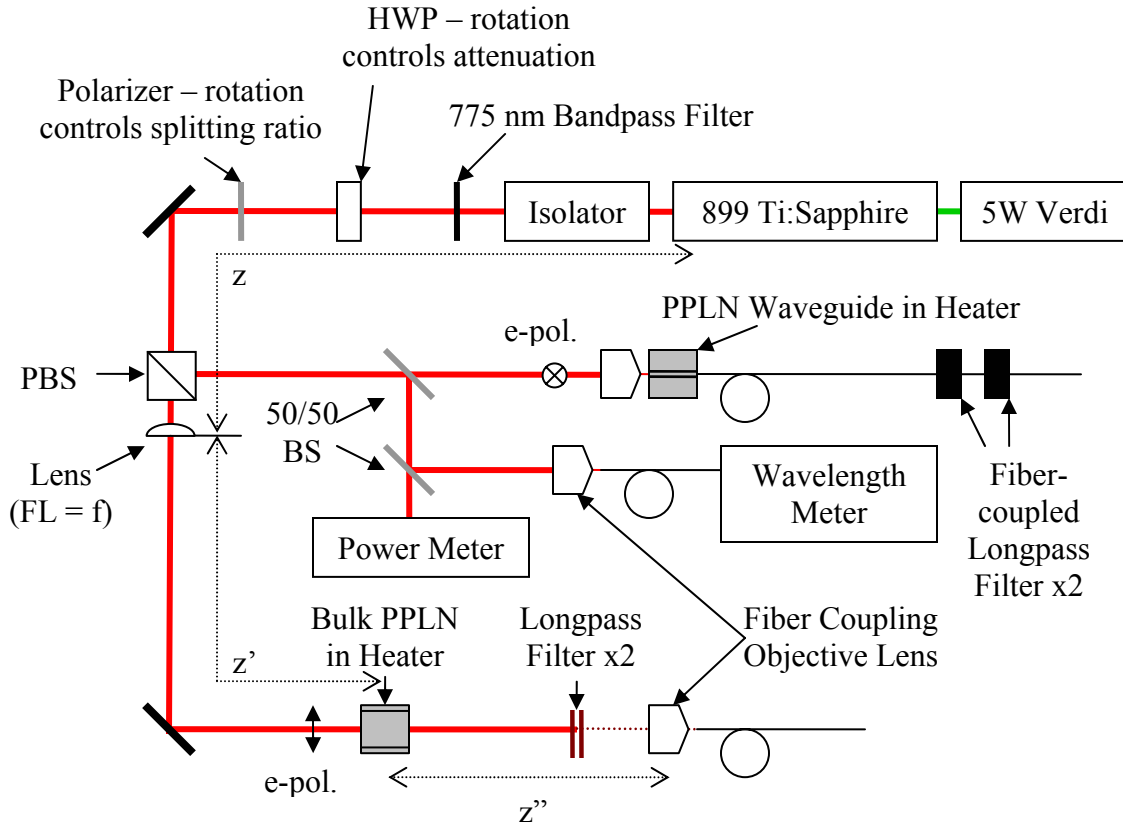


**Figure 3-1: Free-space portion of the experimental setup**

A half waveplate and polarizer, followed by the PBS, are used to vary the attenuation of the pump and to set the ratio of light divided between the waveguide and the bulk crystals. The rotation angle of the polarizer can be used to set the splitting ratio because it determines the polarization of the pump at the PBS. This ratio is not particularly important, because the experiment uses only one of the two sources at a time, but is set to transmit most of the light to the bulk crystal portion of the setup. The power meter, wavelength meter and PPLN waveguide operate with tens of microwatts to low milliwatt levels of light, so the splitting ratio is set to reflect about 4% of the light to this portion of the setup. Once the polarizer angle is set, the half waveplate can be rotated to adjust the laser power by changing the pump polarization hitting the polarizer. The positions of the lenses in the bulk PPLN portion of the setup are set according to the parameters given in Table 3-1. The long focal length lens, either 300 mm or 500 mm, is a 25-mm-diameter Newport Plano-Convex Lens with AR.16 antireflection coating. The fiber-coupling objective, as mentioned earlier, is a Newport F-L10B multi-element lens with a 12 mm

focal length. The HP 86120B Multi-wavelength Meter is designed to accept a 9  $\mu\text{m}$  core input fiber. A Newport M-10x microscope objective with a 14.8 mm focal length, placed 1.5 m from the Ti:Sapphire beam waist, is used to approximately match the laser light to the 0.13 numerical aperture (NA) of the fiber.

The output end of the waveguide is fiber-coupled, so a focusing objective is only needed at the waveguide input. The input end of the waveguide is not fiber coupled because of concerns about how the 775 nm light would couple from the fiber into the waveguide when both are multimode at this wavelength. The waveguide has an elliptical mode approximately 12  $\mu\text{m}$  by 5  $\mu\text{m}$ , so optimal coupling requires a cylindrical lens. However, a New Focus 10x aspheric lens with a 15.4 mm focal length can be used to obtain a coupling efficiency of  $\sim 12\%$ . Positioning the lens 1.5 m from the Ti:Sapphire beam waist, results in a 6  $\mu\text{m}$  beam diameter at the input to the waveguide. This coupling efficiency is sufficient considering the very low power requirements of the waveguide.

Although a cylindrical lens is not used in the setup, it may alleviate one of the problems encountered when using the waveguide. When the waveguide is heated, it is very difficult to stabilize the pump power coupled into the waveguide. With the crystal set to 23°C, just above room temperature, the power coupled into the waveguide fluctuated by approximately  $\pm 5\%$  over a 1 hour period with a  $\pm 2\%$  fluctuation in the laser power itself. This fluctuation of coupling efficiency increased with waveguide temperature and no long-term coupling could be achieved at temperatures above  $\sim 50^\circ\text{C}$ .

The best way to minimize these fluctuations is probably to change the heater packaging. This is not possible for the waveguide used in these experiments because the manufacturer glued the waveguide into the heater to prevent damage to the fiber-coupled end. The heater currently contacts only the bottom side of the crystal, with the waveguide located on the top of the crystal. Additionally, the input end of the crystal extends  $\sim 4$  mm beyond the heated surface. A 25 mm by 5 mm slit for coupling light into the waveguide is cut into the front of the box containing the heater and crystal. It is unlikely, given this design, that the entire crystal is heated uniformly, particularly at high temperatures. The crystal length and position change slightly as the crystal heats and cools, so a second box was built to try to reduce temperature fluctuations resulting from airflow in the room. This did not have a significant impact on the fluctuations in the coupling efficiency and the intermittent heating cycles or the local airflow are most likely the

reasons a stable equilibrium could not be reached. It is clear that changes to the packaging should be made for future waveguides that do not have both ends fiber coupled. It is also possible that using a cylindrical lens to improve the mode-matching could reduce the power fluctuations somewhat. The waveguide is operated near room temperature in all experiments to minimize the power instabilities.

Finally, at the output, the 775 nm pump light must be filtered out while minimizing the loss at 1.55  $\mu\text{m}$ . Suitable long-pass filters with flat transmission over the entire 1450–1650 nm fluorescence bandwidth are only found as free-space components. Following the bulk crystal, a dielectric long-pass filter is used to reflect  $\sim 99.9\%$  of the 775 nm light while transmitting 87% of light between 1450 nm and 1650 nm. This filter reflects wavelengths below 1100 nm and is made by OFC, now a division of Corning. A second filter, a Schott RG-1000 colored glass filter, is used to absorb the rest of the 775 nm light. This filter has 88% transmission between 1450 nm and 1650 nm and  $< 10^{-5}$  transmission at 775 nm. The output of the waveguide is fiber coupled, so two of the RG-1000 filters are placed in the removable filter holder of a RFF-11, a fiber-coupled filter holder made by OZ Optics.

The photons are split between the two detectors using one of the three setups shown in Figure 3-2. The setup shown in Figure 3-2 (a) does not perform a frequency measurement of the photons, but is used for alignment and tests of the optimal pair generation rate, which is discussed in section 3.3. The two advantages of this setup are its high intensity of photon pairs, since the entire output bandwidth is coupled into the detectors, and the elimination of the need to match the filter wavelengths to conjugate frequencies. The broad bandwidth of the photons, however, also makes it difficult to calculate the fiber coupling efficiency, because the detection efficiency changes considerably over the fluorescence bandwidth. Additionally, the 50/50 splitter may send both photons from a pair to the same detector. The detectors can only count a single photon, but the probability of registering a count when there are two incident photons is higher than when there is only a single photon. The statistics for singles and coincidence detections using setup (a) is considered further in section 3.3.

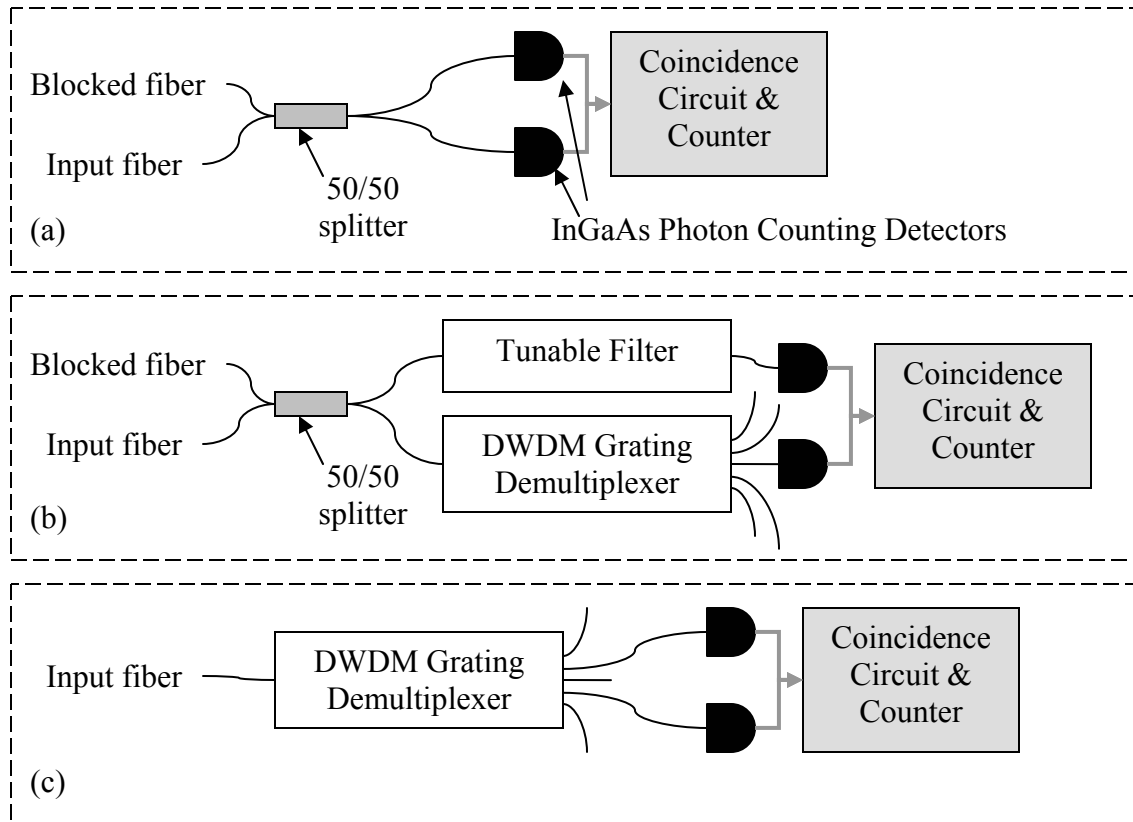


**Figure 3-2: Fiber portion of the experimental setup**

The setups in Figure 3-2 (b) and (c) both perform frequency measurements. The tunable filter is a JDS Uniphase TB9-0126 grating filter with a range from 1460 nm to 1575 nm and a spectral bandwidth of  $\sim 0.55$  nm. The filter's digital reading of central wavelength was found to be accurate to  $\sim 0.1$  nm. The insertion loss and bandwidth were calibrated as a function of the central wavelength and were found to vary smoothly by  $\sim 20\%$  over the 1460 nm to 1575 nm range. The grating demultiplexer is an 8 channel telecommunications component made by APA Optics. The channels are separated by 200 GHz, or  $\sim 1.6$  nm, and have a spectral bandwidth and shape similar to the JDS Uniphase TB9-0126. The center wavelengths of the channels range from 1544.6 to 1555.8 nm. The crosstalk is less than -25 dB between adjacent channels and -30 dB between non-adjacent channels, so the filter has a much sharper roll-off than standard, Lorentzian-shaped filters.

Setup (b) allows a detailed study of the frequency correlation because the tunable filter wavelength can be scanned at any desired resolution. Unfortunately, the 50/50 splitter does not

always split the two photons in a pair. Setup (c) solves the splitting problem by using the grating demultiplexer to always separate the photons. The demultiplexer, however, cannot be tuned and it projects both of the photons into fixed-frequency spectra. The pump wavelength could be scanned in order to study the frequency correlation using setup (c), but we first consider setup (b).

Half of the time, the 50/50 splitter in setup (b) sends both photons from a pair to the same detector. However, if the filters are set to non-degenerate frequencies, the passing of one photon through the filter projects the paired photon into the conjugate frequency, which is then blocked by the filter. Therefore, a detector never sees both photons from a pair.

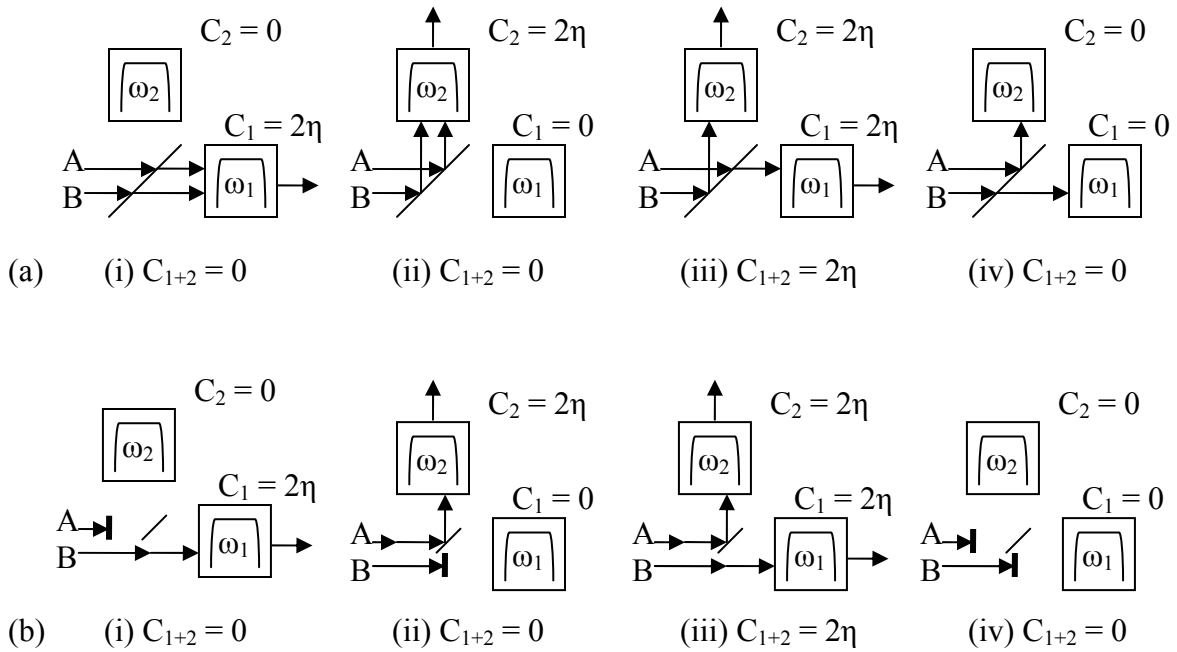


**Figure 3-3: Equivalence between a (a) 50/50 splitter and a (b) frequency splitter with 3dB insertion loss**

This blocking of paired photons makes the 50/50 splitter equivalent to a frequency splitter with 3dB loss, where the photons are split according to whether they are greater than or less than the degenerate frequency. This equivalence is shown in Figure 3-3 where the frequency of photon A is greater than the frequency of photon B. The photons are not generated with these

definite frequencies, but we can label the photons after a measurement is performed in order to enumerate the possible scenarios.

The variables  $C_1$  and  $C_2$  are the single counting rates and the variable  $C_{1+2}$  is the coincidence counting rate. The probability a photon from the entire fluorescence bandwidth passes through a filter is  $\eta$  and the filters are arranged so that  $\omega_2 > \omega_1$ . The coincidence rate is given for the case where the filters are square, have the same  $\eta$  and are set to conjugate frequencies, although these conditions are not required for the equivalency.

Each of the cases, shown in (i) through (iv), has a  $\frac{1}{4}$  probability of occurring. Cases (a)(i) and (a)(ii) show both photons exiting the same arm of the 50/50 splitter. The single counting rate in this case is twice  $\eta$  because there are two photons at different wavelengths, each with a probability  $\eta$  to pass through the filter and zero probability of both passing through the filter. The coincidence rate is always zero when the two photons exit the same way. These cases are equivalent to (b)(i) and (b)(ii), where one of the two photons is lost in the frequency splitter + 3 dB loss. Cases (a)(iii) and (b)(iii) represent the situation where photon A splits into the arm with filter  $\omega_2$  and photon B splits into the arm with  $\omega_1$ . The probability of the photons passing through the filters is twice  $\eta$  because this case dictates that the photon with frequency greater (less) than degeneracy is traveling toward the filter with frequency greater (less) than degeneracy. The number of coincidence counts that occur in this case depends on the shape of the filters and whether they are set to conjugate frequencies, with the maximum number of coincidences occurring for square, conjugate frequency filters. Case (a)(iv) represents the situation where photon A splits into the arm with filter  $\omega_1$  and photon B splits into the arm with  $\omega_2$ . The filters then block both of the photons. Equivalently, case (b)(iv) represents the loss of both photons in the frequency splitter + 3 dB loss.

We can now see that fiber setups (b) and (c) in Figure 3-2 produce the same results, except for the 3dB loss in setup (b). Scanning the pump wavelength can change experimental conditions such as the fluorescence spectrum and the fiber coupling efficiency, in addition to being more difficult than changing the digitally controlled tunable filter. Therefore, setup (b) is used to measure the frequency correlation as a function of filter wavelengths, as discussed in section 4.2. The counting rate statistics discussed in section 4.3, however, is only measured with the filters optimized to pass correlated frequencies. Therefore, by always keeping the pump wavelength set to split correlated frequencies in the grating demultiplexer, we may use setup (c)

to improve the measurement of the photon counting statistics by not suffering the 3 dB loss of a 50/50 beamsplitter.

In addition to measuring the frequency correlation, we would like to measure the fiber coupling efficiency. For these experiments, we are not concerned with the percentage of the total downconversion coupled into the fiber, but with the conditional probability that both photons are coupled into the fiber given that one photon is coupled. The simplest way to measure this is using a setup similar to that in Figure 3-2 (b) with the grating demultiplexer replaced by a wide bandwidth filter. The 0.55 nm bandwidth of the JDS Uniphase TB9 projects the correlated photon into a similarly narrow spectral bandwidth. If the filter in the second arm is much wider than this projected bandwidth, it acts simply as a constant insertion loss. We may then compare the number of coincidence counts to the number of single counts following the TB9. After accounting for insertion losses and the non-unity detection efficiency following the wide bandwidth filter, we can then calculate the conditional fiber coupling efficiency. The wide bandwidth filter used for this purpose is a 3 nm wide tunable filter from Koshin Kogaku (FC-1560-CK10). The insertion loss varies by less than 0.5 dB across a 1 nm bandwidth near the filter’s central wavelength.

<b>Component</b>	<b>Insertion Loss (dB)</b>
Long-pass filters (bulk setup) + F-L10B lens	-1.4
Long-pass filters (waveguide setup) + OZ Optics holders	-1.6
50/50 splitter (excess only)	-0.36
JDS Uniphase TB9 tunable filter	-2.2
APA Optics grating demultiplexer	-3.5
Koshin Kogaku FC-1560-CK10	-1.6

**Table 3-2: Insertion loss of components at 1550 nm**

Finally, we must measure all of the insertion losses in the experiment in order to accurately measure the fiber coupling efficiency and the photon statistics following the spectral filters. The insertion loss can be measured classically using a laser and a power meter. The HP 8168A tunable laser and two different power meters are used to measure the insertion loss. The HP 81532A power meter module in an HP Lightwave multimeter (HP 8153A) is used for fiber coupled components and the Coherent Ultima Labmaster with a 33-0944 germanium sensor is used for free space measurements. The measured insertion losses are listed in Table 3-2. The insertion losses were measured from 1540 nm to 1560 nm and found to be flat to within ~2% for all components tested. Additionally, the 50/50 splitting ratio was found to be 50%  $\pm$ 0.2% over this range.

### **3.2 Crystal Temperature Optimization**

As mentioned in section 2.3, the temperature of the PPLN crystal can be adjusted to vary the phasematching conditions and correct for any errors in the poling period. Therefore, we must experimentally find the temperature corresponding to degenerate phasematching. We would also like to confirm the predictions about the bandwidth and the phasematching versus temperature curve (Figure 2-5). We may do this by measuring the conversion efficiency of the crystal as a function of wavelength and temperature. This is done using the free space experimental setup shown in Figure 3-1, the JDS Uniphase TB9 tunable filter and a single detector. This measurement uses focusing arrangement #1, given in Table 3-1, to maximize the signal to noise ratio of this measurement. A schematic for the experimental setup of this measurement is shown in Figure 3-4.

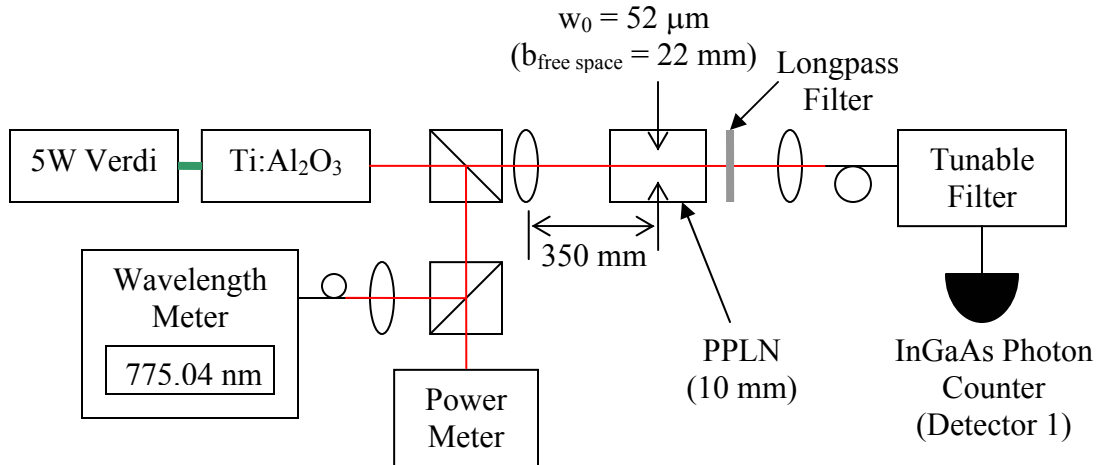


**Figure 3-4: Schematic of the experimental setup for the conversion efficiency measurement**

After the crystal and two lenses have been arranged, the fiber position is optimized in three steps. First,  $1.55 \mu\text{m}$  light from a laser is sent into the fiber and focused backwards into the PPLN crystal. The coupling lens position is adjusted so the  $1.55 \mu\text{m}$  light matches the beam path of the  $775 \text{ nm}$  laser. As mentioned in section 3.1, the second harmonic generation (SHG) of  $1.55 \mu\text{m}$  light and our degenerate parametric fluorescence process both involve the same three frequencies, so the phasematching conditions and nonlinear coefficient for both processes are the same. We can therefore use a sensitive Si detector to measure the SHG after the crystal to optimize the distance between the coupling lens and fiber.

The second step is to disconnect the fiber from the  $1.55 \mu\text{m}$  laser and unblock the  $775 \text{ nm}$  pump beam. The output in the fiber is measured using the highly sensitive power meter module (HP 81532A) in an HP Lightwave multimeter (HP 8153A). The crystal temperature and fiber position are adjusted to maximize the downconversion in the fiber.

Finally, the output fiber is connected to a 50/50 splitter. The outputs from the splitter are connected to the two photon counting detectors and the coincidence circuit is optimized as discussed in section 2.2. Final tweaking of the fiber position is performed to optimize the coincidence counting rate. By optimizing the coincidence rate, we can be sure that the coupled mode is collinear with the pump beam, as is the case in the frequency correlation experiments.

We now disconnect the 50/50 splitter and arrange for the conversion efficiency to be measured using the setup shown in Figure 3-4. The counting rate and laser power are recorded at each wavelength and temperature combination. The conversion efficiency, per nm of output

bandwidth, is then calculated accounting for the insertion losses, pump power, dark count rate, detection efficiency and variations in the filter bandwidth. The results of these measurements are shown in Figure 3-5.

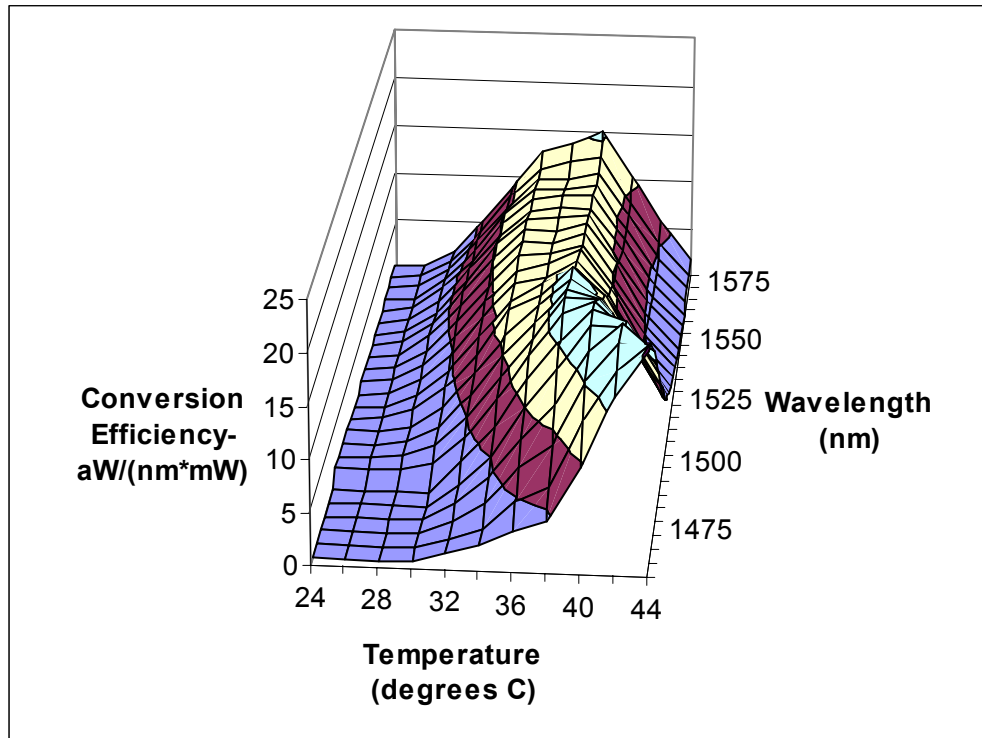


**Figure 3-5: Conversion efficiency per nm of output bandwidth as a function of crystal temperature and fluorescence wavelength**

The poling period used to calculate the phasematching curve shown in Figure 2-5 was selected to match the experimental data shown in Figure 3-5, allowing an excellent fit between theory and data. The temperature at which degenerate phasematching occurs in PPLN is very sensitive to the poling period with a 0.01% change in the poling period resulting in a 0.5°C change in the degenerate phasematching temperature. The intended 19 μm poling period differs from the calculated poling period of 18.984 μm by only 0.084%. It is also possible that the poling period is correct and the difference is between the true temperature dependent index of refraction and one calculated using Sellmeier equations. Looking at just the 34°C curve near degeneracy (Figure 3-6), we can see that the FWHM of the process is close to the bandwidth calculated in section 2.3.

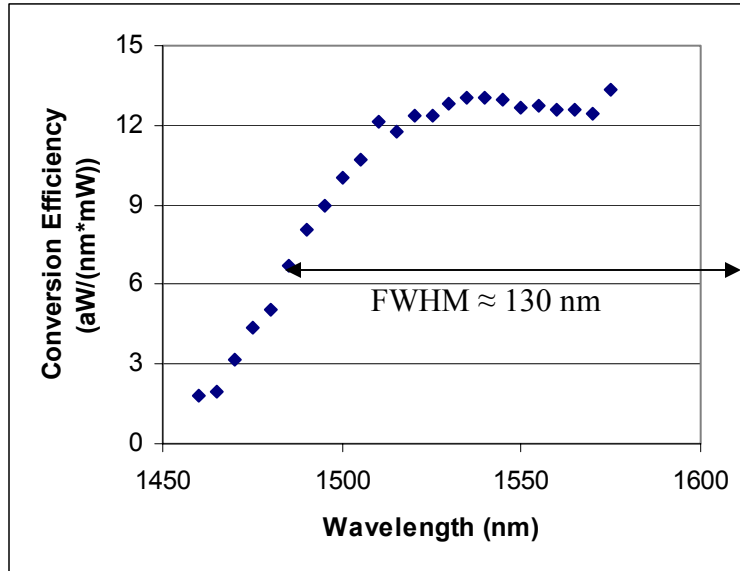


**Figure 3-6: Conversion efficiency per nm of output bandwidth at crystal temp = 34°C**

### **3.3 Pair Generation Rate Optimization**

The final optimization we must consider is how to set the pair generation rate. This rate should be set to minimize the background coincidences. When the pair generation rate is low, the background is dominated by coincidences between dark counts. Conversely, a high pair generation rate results in the background being dominated by coincidences between uncorrelated photons produced in the parametric fluorescence process. The goal is to optimize the coincidence signal to noise ratio.

To avoid confusion with the signal detector rate, the coincidence signal rate is called the data. This data rate is the rate at which both photons of an entangled pair are detected, producing a coincidence count. The error rate, the noise in the coincidence rate, is any coincidences that are not the result of detecting both photons from an entangled pair. Four detector parameters affect the performance of the system: detection efficiency, repetition rate, dark count probability and jitter. In addition to the detectors, the pair production rate and insertion losses also affect the system's performance. For this analysis, all noise is considered to have Poisson statistics and is attributed to either uncorrelated photon pairs or dark counts. Furthermore, the production of pairs is approximated as a Poisson process, although it actually has Bose-Einstein statistics. The afterpulse probability is considered to be negligibly low.

The detector performance has already been considered in sections 2.1 and 2.2. The pair production rate and system losses must now be considered. The mean number of pairs generated per gate can be calculated using a procedure described in reference [16], where the coincidence rate and both single detector rates are used to infer the pair generation rate. This procedure can also be used to determine the total losses in the system. In order to apply this calculation to the low photon fluxes we are considering, we must perform background subtraction. The background for the single detector rate is simply the dark count rate. The coincidence background is the rate of coincidences that do not result from the detection of both photons from a pair, namely the error rate we are considering in this section. This rate can be measured by moving the gating pulses and SCA window as described in section 2.2. The three rates can therefore be expressed as:

$$Counts_1 = \frac{S_{1,signal}}{1 - S_{1,signal} / R_{gating}} - S_{1,dark} = p(cnt_1 | pair) N_{pair/gate} R_{gating} \quad (3-9)$$

$$Counts_2 = \frac{S_{2,signal}}{1 - S_{2,signal} / R_{gating}} - S_{2,dark} = p(cnt_2 | pair) N_{pair/gate} R_{gating} \quad (3-10)$$

$$\begin{aligned} Counts_{coinc} &= \frac{S_{coinc,signal} - S_{coinc,backgrd}}{(1 - S_{1,signal})(1 - S_{2,signal})} \\ &= p(split)p(cnt_1 | pairsplit)p(cnt_2 | pairsplit) N_{pair/gate} R_{gating}, \end{aligned} \quad (3-11)$$

where  $Counts_{channel}$  is the background corrected counts on channel = {1,2,coinc},  $S_{channel,signal}$  is the counts measured on channel = {1,2,coinc},  $S_{chan,dark}$  is the dark counts measured on channel = {1,2},  $S_{coinc,backgrd}$  is the background coincidences,  $R_{gating}$  is the gating repetition rate and  $N_{pair/gate}$  is the mean number of pairs produced per gate. The scale factor,  $1/(1 - S_{channel,signal} / R_{gating})$ , corrects for the fact the detector can only count one event per gate, although it is a small correction for the data in this thesis. The probability of multiple dark counts within a gate is small enough to neglect a similar correction to the dark counts.

The probability of the pair splitting,  $p(split)$ , is  $\frac{1}{2}$  for the setup shown in Figure 3-2 (a). It should be noted that the conditional probability of counting a photon given that the two photons are split into different channels is not exactly equal to the conditional probability of counting a photon given only that pair is generated, as assumed in reference [16]. If it is not known whether

the pair split, each channel has a 25% chance of receiving no photons, a 50% chance of receiving one photon and a 25% chance of receiving two photons. The photon counters can only resolve one event at a time, so the conditional probabilities are related by:

$$p(cnt_{channel} | pair) = p(cnt_{channel} | pairsplit) \left[ 1 - \frac{p(cnt_{channel} | pairsplit)}{4} \right]. \quad (3-12)$$

As the conditional probability of detection approaches zero (low detection efficiency or high system losses), the two probabilities become equal because the detector registers twice as many counts given two photons as it does given one photon. If the splitting includes non-degenerate filters, as in Figure 3-2 (b) and (c), the two conditional probabilities are equivalent. Equation (3-12) is actually two equations, so we can use equations (3-9) through (3-12) to solve for the five unknowns: the mean number of pairs generated per gate ( $N_{pair/gate}$ ) and the four conditional probabilities.

The expected data and error rates can be expressed in terms of the parameters discussed above. Assuming the detector jitter is much smaller than the gate interval and assuming the fiber and electronic path lengths are matched so that coincident detections are centered in the SCA window, we can calculate:

$$R_{Data} = R_{gating} (1 - e^{-N_{corvents/gate}}) \frac{N_{pair/gate} p(cnt_1 | split) p(cnt_2 | split)}{2 N_{corvents/gate}} \quad (3-13)$$

$$N_{corvents/gate} = N_{pair/gate} \left[ p(cnt_1 | pair) + p(cnt_2 | pair) - \frac{p(cnt_1 | split) p(cnt_2 | split)}{2} \right] + N_{dark,1/gate} + N_{dark,2/gate} \quad (3-14)$$

and

$$R_{Error} = R_{gating} (1 - e^{-N_{uncorvents/gate}}) \left[ \frac{N_{pair/gate} p(cnt_1 | pair) + N_{dark,1/gate}}{N_{uncorvents/gate}} \left( 1 - e^{-\frac{\Delta SCA}{2\Delta gate} (N_{pair/gate} p(cnt_2 | pair) + N_{dark,2/gate})} \right) + \frac{N_{pair/gate} p(cnt_2 | pair) + N_{dark,2/gate}}{N_{uncorvents/gate}} \left( 1 - e^{-\frac{\Delta SCA}{2\Delta gate} (N_{pair/gate} p(cnt_1 | pair) + N_{dark,1/gate})} \right) \right] \quad (3-15)$$

$$N_{uncorvents/gate} = N_{pair/gate} [p(cnt_1 | pair) + p(cnt_2 | pair)] + N_{dark,1/gate} + N_{dark,2/gate}, \quad (3-16)$$

where  $R_{\text{gating}}$  is the repetition rate of the detectors,  $N_{\text{dark,chan/gate}}$  is the mean number of dark counts per gate on channel = chan={1,2}, and  $\Delta\text{SCA}/\Delta\text{gate}$  is the length of the coincidence window relative to the total gate interval.

The equations are derived by enumerating the sources of photon counts, which are referred to as events. We consider coincidences between paired photons as a single event so that we are considering only Poisson processes. This allows us to find the total rate by adding together the rates of each separate process. The rates, including all events, are given by  $N_{\text{correvents/gate}}$  when we are including true coincidences and  $N_{\text{uncorrevents/gate}}$  when we are considering only background coincidences. The difference in rates comes from the fact we are combining both photon counts into a single event when they result in a true coincidence count.

The data and error rates can then be calculated by multiplying the gate repetition rate,  $R_{\text{gating}}$ , the probability of one or more events within a gate,  $(1-e^{-N})$ , and the probability that a coincidence occurs given an event. This final probability can be calculated simply by dividing the rate at which coincidences occur by the total event rate, since we are splitting Poisson processes. The data, or true coincidence, rate is the product of the pair generation rate,  $N_{\text{pair/gate}}$ , the  $\frac{1}{2}$  probability of splitting a pair and the two conditional probabilities of detection, as first given in Equation (3-11).

The errors, or background coincidences, have two independent sources. The counts resulting in background coincidences are uncorrelated, so either detector 1 or detector 2 fires first and this is considered the event. A coincidence occurs if the other detector also fires within the coincidence window. It was assumed that the coincidence window is centered on simultaneous events, so there is half the window remaining for the other detector to create a false coincidence. The dark counts and true photon counts are indistinguishable, so these two processes are combined for simplicity. The coincidence signal to noise can be calculated by taking the ratio  $R_{\text{Data}}/R_{\text{Error}}$ . These predictions are confirmed experimentally in section 4.1 for both the waveguide and bulk crystals.

## CHAPTER 4 - EXPERIMENTAL RESULTS

### ***4.1 Bulk and Waveguide Crystal Comparison***

Given the noisy, slow detector performance, the primary consideration for choosing between the bulk and waveguide crystals for use in laboratory experiments is the achievable signal to noise ratio. Although the waveguide achieves much higher conversion efficiencies, low conversion efficiency can be compensated in the lab by increasing the pump power. Loss after the pairs are generated, however, cannot be compensated and it reduces the coincidence rate from correlated photons. Therefore, we choose the crystal that minimizes the losses following the generation of photon pairs in order to maximize the coincidence signal to noise ratio.

The crystal choice affects three different types of loss. First, both crystals have a propagation loss inside the crystal. This propagation loss is only due to absorption in the bulk crystal and is negligible compared to other losses. The waveguide, however, has propagation loss that is due to the coupling of the guided mode into the cladding. This waveguide loss is ~8% for 1550 nm light traveling the entire 10 mm crystal length, according to the specifications given by HC Photonics.

The second source of loss is the efficiency with which the fluorescence output can be coupled into a fiber. As discussed in section 3.1, we are only concerned with losing photons when the conjugate photon is coupled into the fiber. The coupling efficiency in the bulk crystal is related to the spatial overlap of the signal and idler photons in the collected output mode. Although a calculation to predict this coupling efficiency estimates ~89%, a lower coupling efficiency is found experimentally in section 4.3. Any reflections at the interface between the crystal and air should also be considered. However, the PPLN crystal is anti-reflection coated for 1550 nm and any reflections are negligible.

The waveguide has only a single spatial mode, so the coupling efficiency should simply be the level of mode matching between the waveguide and the fiber modes, along with the loss due to reflections at the uncoated interface between the waveguide and the output fiber. The elliptical output mode of the waveguide must be transformed in order to match the circular mode of the fiber. HC Photonics designed and assembled the fiber couple and the details are not available, although the specifications estimate 84% mode matching. The total loss due to reflections at the interface between the waveguide and the fiber is specified to be 18%. These

specified losses in the waveguide are consistent with transmission measurements made by connecting a 1.55  $\mu\text{m}$  laser to the fiber-coupled end of the waveguide and detecting the light that exits the free-space end. Finally, the waveguide and bulk setups have a slightly different loss due to the long-pass filters. Although this is not an inherent loss, it is reflected in the signal to noise ratios for the two setups, so it must be considered when we compare them. The insertion loss for the fiber coupled filters, given in Table 3-2, is just 0.2 dB more than the insertion loss for the long-pass filters and coupling lens used in the bulk crystal setup. This difference is considered in our final analysis, but it is clear that the filters have only a small impact on which source achieves a higher signal to noise ratio.

In section 3.3, we developed formulas to calculate the expected signal to noise ratio given the detector performance and the losses in the system. Although we have tried to account for many of the losses, the total system loss can be measured more accurately using the procedure involving single and coincidence counting rates that is outlined in section 3.3. The signal to noise ratio can also be found experimentally by measuring the correlated coincidence rate and the background coincidence rate. Measuring the background coincidence rate is very time consuming, particularly when the pair generation rate is low and the background is dominated by coincidences between dark counts. Therefore, we would like to show good agreement between the calculations and the measured signal to noise ratio so that we do not need to optimize the pair generation rate experimentally each time the insertion loss is changed.

The signal to noise ratio is measured for several pair generation rates in both the waveguide and the bulk crystal. Coupling the 775 nm pump into the waveguide is difficult when it is heated, as discussed in section 3.1, so the pump wavelength was adjusted to 776.63 nm to allow degenerate phasematching with the waveguide crystal at 23°C. This pump wavelength was also used for testing the bulk crystal for consistency. Obtaining degenerate phasematching in the bulk crystal with the pump at 776.63 nm required heating the bulk crystal to 62°C. Focusing arrangement #2, given in Table 3-1, is used to couple the fluorescence from the bulk crystal into the fiber. The splitting of photons in the fiber is performed using just a 50/50 splitter, as shown in arrangement (a) of Figure 3-2. Unfortunately, the detection efficiency is not known across the entire fluorescence bandwidth, so using the 50/50 splitter without a spectral filter makes predicting the system loss difficult. The alternative is to spectrally filter a portion of the fluorescence bandwidth so that the detection efficiency is well-defined, but this reduces the

effective pair generation rate for a given pump power. The decision not to use a spectral filter was made because it would be difficult to produce high pair generation rates given the available narrowband filters and the  $\sim 100$  mW maximum pump power.

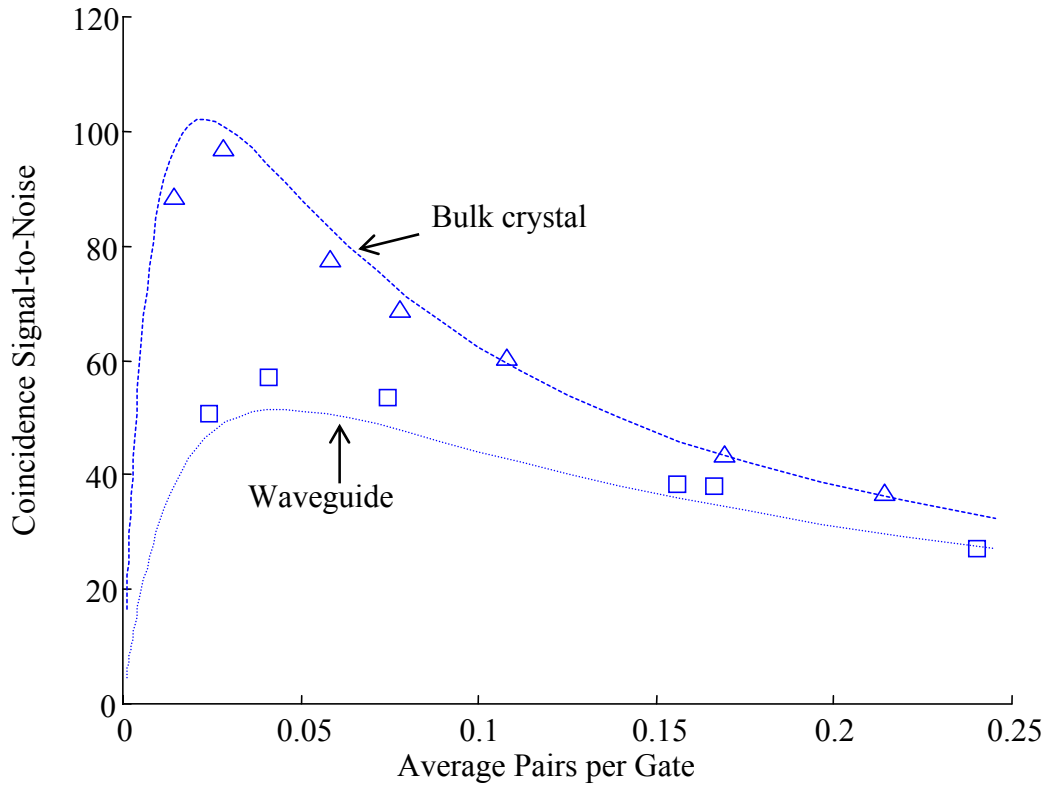


**Figure 4-1: Theoretical (lines) and experimental (shapes) coincidence signal to noise ratio for bulk and waveguide crystals**

The coincidence signal to noise ratio measurements are shown in Figure 4-1 as squares for the waveguide and triangles for the bulk crystal. The pump power used to make these measurements ranged from  $25 \mu\text{W}$  to  $125 \mu\text{W}$  for the waveguide and from  $500 \mu\text{W}$  to  $4 \text{mW}$  for the bulk crystal. The power coupled into the waveguide was estimated to be  $\sim 12\%$  of that measured before the coupling lens. The pair generation rates associated with these data points were simply the detector 1 counting rate divided by  $p(\text{cnt}_1|\text{pair})$ , as defined in section 3.3. This conditional probability of detection is simply a measure of the total system loss. One measurement of the coincidence and single detector count rates, made before collecting the other

data, is used to calculate the conditional probabilities of detection. These detection probabilities are also used to calculate the theoretical curves shown in Figure 4-1. The good agreement of data and theory verify that just a single data point can be used to accurately measure the system loss and determine the optimal pair generation rate.

Although the waveguide has much higher conversion efficiency than the bulk crystal, the bulk crystal clearly allows a better signal to noise ratio than the waveguide and is used in all further experiments. This is a result of the lower conditional probability of detection in the waveguide setup. It is not clear, given the calculation of the bulk crystal coupling efficiency in section 4.3, why the bulk crystal has a better conditional probability of detection, so we reexamine this question in section 5.2.

## **4.2 Frequency Correlation Demonstration**

We may now confirm the spectral quantum magic bullet effect by showing how a narrowband filter measurement of the signal photon projects the idler photon into the conjugate, narrowband spectrum. This experiment is performed using the fiber setup shown in Figure 3-2 (b), with the TB9 tunable filter and grating demultiplexer in opposite arms following the 50/50 splitter. The transmission curve for each of the grating demultiplexer channels is measured using the HP 8168A tunable laser and the HP 81532A power meter module. We measure the single detector and coincidence counting rates as a function of the TB9 center frequency. The single detector count rate should be constant for all filter settings because we expect photons with wavelengths over the entire fluorescence bandwidth. However, according to the spectral quantum magic bullet effect, we expect the coincidence counting rate to peak only when the TB9 filter is set to the frequency that is conjugate to the demultiplexer channel we are using.

This experiment is again performed with focusing arrangement #2, with the pump wavelength set to 776.63 nm and with the crystal temperature set to 62°C. Channel 5 of the grating demultiplexer has a center wavelength of 1551.0 nm and should project the conjugate photons to a bandwidth centered at 1555.5 nm. The filter wavelength was scanned from 1549 nm to 1557 nm and the coincidence and single detector count rates are measured for 5 minutes at each filter setting. The results of this measurement, shown in Figure 4-2, clearly demonstrate the quantum magic bullet effect.

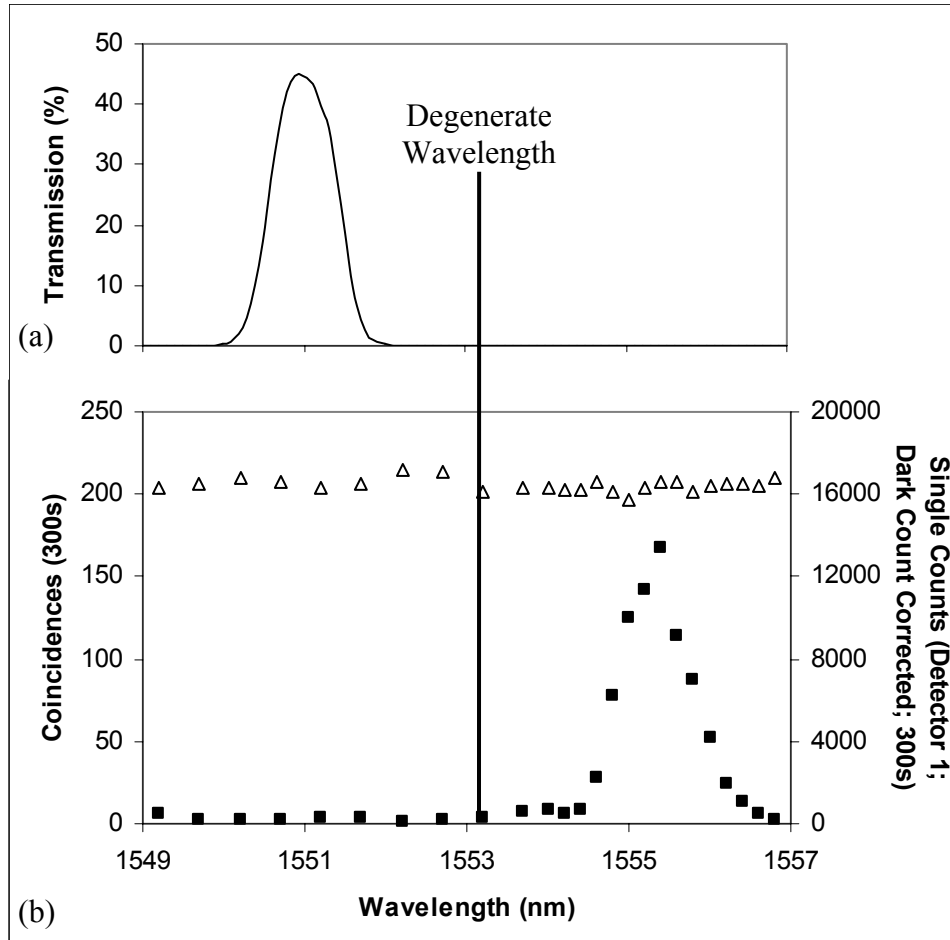


**Figure 4-2: (a) Transmission curve for grating demultiplexer channel 5; (b) Counts over 300 second period for single detector (open triangles) and coincidences (filled squares) as a function of tunable filter wavelength**

This experiment can be repeated with the other channels of the grating demultiplexer to verify that these frequency correlations exist for any pair of conjugate frequencies within the fluorescence bandwidth. The correlations are shown across an 8 nm bandwidth in Figure 4-3, although correlations could also be measured over the entire >100 nm fluorescence bandwidth. This incredible range of correlations exists because frequency is a continuous variable. This demonstration clearly shows that continuous variables may permit a broader range of applications than discrete variables, such as polarization. Some of the ongoing research involving continuous variables are discussed briefly in section 5.2.

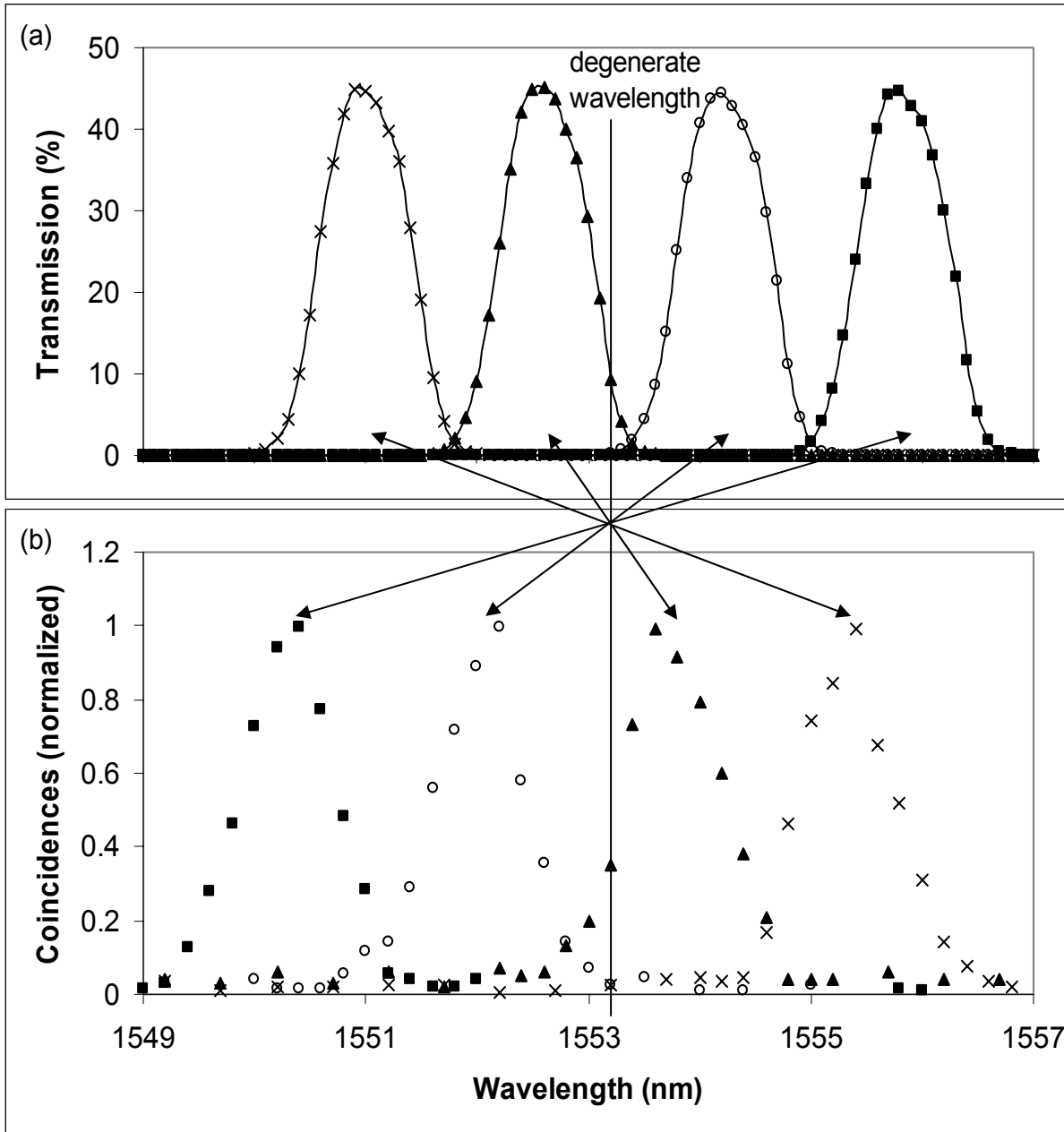


**Figure 4-3: (a) Transmission curve for grating demultiplexer channels 5-8; (b) Normalized coincidence rate as a function of tunable filter wavelength**

### **4.3 Detected Light Statistics**

Finally, we would like to measure the probability of obtaining a coincidence count when conjugate, equal bandwidth spectral filters are placed in the signal and idler arms. The best

measure of this correlation between the signal and idler channels is the normalized photocount variance, which is defined in reference [7] as:

$$\sigma_N^2 = \frac{\langle (\hat{N}_S - \hat{N}_I)^2 \rangle}{\langle \hat{N}_S \rangle + \langle \hat{N}_I \rangle}, \quad (4-1)$$

with  $\hat{N}_S$  and  $\hat{N}_I$  representing the number of signal and idler counts over the short coincidence time window. Both  $\hat{N}_S$  and  $\hat{N}_I$  are almost always equal to zero, with a small probability of equaling one and a negligible probability of being greater than one (the photon counters cannot register more than one count during a coincidence window, but this probability would be negligible even if they could register multiple counts). If the signal and idler counts are completely uncorrelated, the normalized photocount variance is approximately one. Conversely, if the signal and idler counts are completely correlated, this variance equals zero. We would like to measure a variance close to zero in order to demonstrate the quantum magic bullet effect, but the low detection efficiency and high losses increase this variance significantly. We can, however, compare this normalized photocount variance to the background photocount variance to show that the difference is statistically significant.

The experimental arrangement for measuring the photocount variance uses focusing arrangement #3 and the fiber setup shown in Figure 3-2 (c), with the grating demultiplexer splitting the signal and idler photons. The signal detector is connected to channel 4 and the idler detector is connected to channel 5 of the grating demultiplexer. The central wavelengths of the channels 4 and 5 were measured to be 1549.392 nm and 1550.998 nm respectively. These measured values are in good agreement with the 1549.353 nm and 1550.960 nm wavelengths listed in the design specifications. The sum frequency of these two filters sets the pump wavelength to be 775.097 nm. The closest stable mode of the Ti:Sapphire laser is 775.063 nm, which is close enough to the sum frequency for there to be excellent overlap of the projected and conjugate filter bandwidths. With the pump set to 775 nm, the bulk PPLN temperature is changed to 34°C to achieve degenerate phasematching.

Both the peak and background coincidence rates are measured during ten intervals, each five minutes long. The normalized photocount variance for true coincidences is found to be 0.99485, with a standard deviation of 0.000322 and the background photocount variance is

0.999945, with a standard deviation of 0.000036. These variances are calculated using the total single and coincidence counts, without any subtraction of dark counts or background coincidences. Using the total single counting rates, we can calculate the photocount variance that should be expected given completely random coincidences. This uncorrelated photocount variance is 0.999948.

Although the photocount variance of  $\sim 0.995$  is far from the zero photocount variance we would like to demonstrate, it is approximately 16 standard deviations from the uncorrelated variance. By comparison, the background photocount variance is just 0.10 standard deviations from the uncorrelated variance. As expected, it is clear from this that we can see significant correlations between the signal and idler channels despite filtering their  $>100$  nm bandwidths using  $\sim 0.5$  nm bandpass filters. This correlation is measured while collecting only a single spatial mode of the downconversion and despite the fact almost half of the single counts are dark counts. The high photocount variance is not surprising considering over 95% of the photons are lost just because of the low detector efficiency and classical insertion losses.

The photocount variance is useful for calculating the level of correlation between the signal and idler channels, but it does not give much insight into the loss in correlations introduced by the spectral filters. In order to isolate the spectral magic bullet effect, we must first account for all of the other losses in the system. We have shown in section 4.1 that all of the system losses can be measured accurately using the single detector and coincidence counting rates. This is the ideal way to measure the loss with and without the filters, assuming we can remove the loss introduced by the narrowband filters without changing any of the other losses in the system.

The setup for isolating the other losses is first described near the end of section 3.1. The key idea is that we can limit the fluorescence bandwidth, so that we do not change the detection efficiency, by putting a narrowband filter in just one of the arms. Considering only the events when the filtered photon is detected, we can measure the conjugate photon's loss without forcing it to pass through its own narrowband filter. Therefore, the setup splits the photons using a 50/50 coupler and sends the signal, or trigger, photon through the narrowband, TB9 tunable filter. The idler photon is sent through a much wider bandwidth filter, since it has been projected into the narrow, conjugate bandwidth of the signal filter. The wide bandwidth filter can be treated as a classical insertion loss and is needed in order to reduce the background counts from uncorrelated

photons. We must be sure that the filters are non-degenerate so the 50/50 splitter can be treated as a simple, 3 dB loss.

There are several contributions to the loss in the idler channel. The detection efficiency was calculated in section 2.2 and the insertion losses of various components are listed in Table 3-2. We have losses from the coupling lens, the long-pass filters, the Koshin Kogaku filter, the 3 dB splitting loss and the excess loss in the 50/50 splitter. Coincidence and single counting rates are measured with the filters set to conjugate frequencies as well as with the center frequencies slightly offset, in order to verify that the wideband filter acts as a near-constant loss. The average ratio of the coincidence to single counts, taken over 20 min intervals, is given in Table 4-1. This experiment was performed immediately following the photocount variance measurement, so the free-space portion of the setup was not touched.

<b>Tunable Filter Wavelength Offset</b>	<b>-0.5 nm</b>	<b>0 nm</b>	<b>+0.5 nm</b>
Coincidences / Singles – Dark Count Corrected	0.0144	0.0158	0.0149
Coincidences / Singles – Background Corrected	0.0136	0.0150	0.0141
Coincidences / Singles – Perfect Detection Efficiency	0.0953	0.105	0.0990
Coincidences / Singles – No Insertion Loss	0.42	0.46	0.43

**Table 4-1: Ratio of coincidences to singles with corrections listed in left column**

The values in the chart may be interpreted as conditional probabilities, with corrections for perfect detection efficiency and no insertion loss giving the conditional probabilities assuming those losses could be removed. The corrections in the chart are cumulative, so the conditional probabilities corrected for insertion loss actually include all of the corrections listed in the chart. The slightly lower conditional probabilities with the filters offset is consistent with the higher loss of the wideband filter at  $\pm 0.5$  nm to each side of the central filter wavelength. It is clear that this filter is wide enough to prevent spectrally filtering the projected idler photon.

The final 46% conditional probability is a measure of all of the losses we have not included in the corrections. One of these losses comes from the true coincidences that are blocked by the narrow coincidence window (Figure 2-3). This is not included in the corrections because the conditional detection efficiencies are calculated assuming the coincidence circuit is

perfect. The noisy detectors required that we use the coincidence window to eliminate as much of the background as possible, so we are losing some of the true coincidences. However, we expect the major additional loss to be the fiber coupling. The fiber coupling efficiency cannot be measured classically for the bulk crystal because the downconversion is produced in many spatial modes. It was predicted to be ~89% in section 3.1, but it appears that it is probably closer to 50-60%.

It may be possible to improve the fiber coupling by finding a better procedure to position the fiber. Optimizing the fiber position is difficult because both the single and coincidence counting rates change with position, and it is their ratio that needs to be maximized. Furthermore, the slow coincidence counting rate makes it difficult to accurately measure this rate. Increasing the pump power helps increase this coincidence rate, but is accompanied by a reduction in the coincidence signal to noise ratio, as shown in Figure 4-1. The signal to noise ratio is still high enough in most cases for the increased pump power to be useful for alignment.

However, removing the tunable filters and using just the 50/50 splitter, to dramatically increase the coincidence counting rate, can actually make alignment more difficult. The total downconverted output power is higher for near-degenerate phasematching than for degenerate phasematching, so removing the filters causes the single detector counting rates to peak for a non-collinear fiber position. Combined with the fact the coincidence signal to noise ratio decreases with all of the additional photon pairs, removing the filters can lead to misleading coincidence counting rates. There is no obvious solution to improving the fiber alignment without faster detectors or careful, time-consuming data collection.

We can now use the losses that have been calculated in Table 4-1 to isolate the loss introduced by putting a narrowband filter in both of the arms. Using the data collected for the photocount variance measurement, the condition probability with various corrections is given in Table 4-2. The components considered for calculating the insertion loss in this setup are the grating demultiplexer, the long-pass filters and the coupling lens.

Coincidences / Singles – Dark Count Corrected	0.0149
Coincidences / Singles – Background Corrected	0.0147
Coincidences / Singles – Perfect Detection Efficiency	0.103
Coincidences / Singles – No Insertion Loss	0.317
Coincidences / Singles – Perfect Coupling Efficiency	0.69

**Table 4-2: Ratio of coincidences to singles with corrections listed in left column**

Excluding all previously measured losses, including the demultiplexer’s insertion loss, we can see that there is almost a 70% chance of the idler photon passing through the spectral filter. If the filters were perfectly square, we would expect this probability to be 100%, but it is clear from the transmission curve of the filter shown in Figure 4-4 that the projected bandwidth experiences additional filtering due to the filter’s sloped edges. This 69% conditional probability is a clear demonstration of the quantum magic bullet effect.

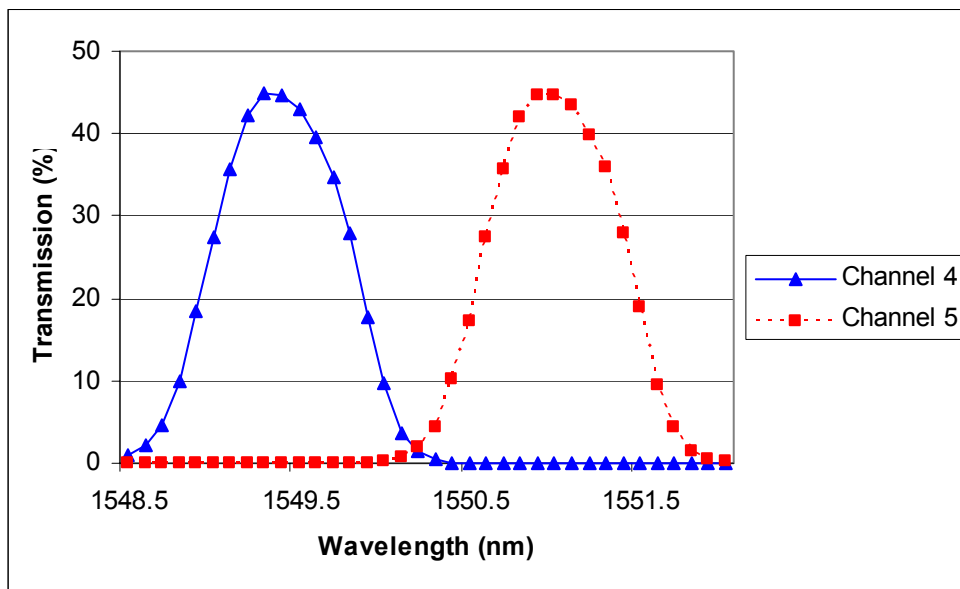


**Figure 4-4: Transmission curve for channels 4 and 5 of the grating demultiplexer**

## **CHAPTER 5 - CONCLUSION**

### **5.1 Technical Achievements**

This thesis is the first detailed study of the spectral quantum magic bullet effect. The frequency correlation of downconverted photons demonstrated here can be combined with the results of previous Hong-Ou-Mandel quantum interference experiments [9] to show that the downconverted photons are indeed frequency entangled. Furthermore, these experiments were performed despite the significant experimental challenges introduced by using two InGaAs APD photon counters. To our knowledge, this is the first time an experiment has used degenerate 1.55  $\mu\text{m}$  photon pairs. This is not surprising considering the low quantum efficiency, high dark counts and slow operation of the detectors. A high signal to noise ratio could only be achieved by carefully optimizing the detectors, the coincidence circuit, the pump power and the fiber coupling of the downconverted photon pairs.

Although the detector limitations prevent a practical commercial system involving photon pairs at 1.55  $\mu\text{m}$ , it has been shown that InGaAs APD photon counters are capable of adequate performance in laboratory demonstrations. Formulas have been derived that allow the pump power to be quickly optimized based on the desired data rate and signal to noise ratio. Furthermore, fiber coupling from a collinear arrangement in bulk PPLN has been demonstrated with high efficiency, comparing favorably to downconversion generated in a PPLN waveguide. The experimental arrangement designed in this thesis is suitable for additional studies of frequency entanglement or tests of quantum communication protocols involving degenerate, 1.55  $\mu\text{m}$  photon pairs.

### **5.2 Concluding Remarks**

In addition to clearly demonstrating the quantum magic bullet effect, this work has drawn several, more functional, conclusions. These conclusions include methods to optimize the detectors, the coincidence circuit and the pair generation rate. However, one of these conclusions, the better performance of the bulk setup compared to the waveguide, needs further examination.

We have measured all of the losses in the waveguide setup, so if we add the propagation, reflection, mode-matching and filter losses, we expect 3.4 dB loss before splitting in the

waveguide setup. The losses in both the bulk and waveguide setups dictate the conditional detection probabilities, so we can solve for the loss in the bulk setup. According to the conditional detection probabilities measured in section 4.1, the loss in the waveguide setup is 1.5 dB higher than in the bulk setup. The bulk setup's loss due to fiber coupling should therefore be 3.4 dB minus the 1.5 dB difference minus the measured 1.4 dB filter insertion loss. By this method, we estimate 0.5 dB fiber coupling loss, or 89% fiber coupling efficiency.

The exact agreement between this measurement and the theoretical prediction in section 3.1 is misleading, because we would at least expect the experimental coupling to include an additional 4% reflection loss. Regardless, this estimate is clearly higher than the fiber coupling efficiency estimated in section 4.3. Although the two coupling efficiency estimates are made for different focusing arrangements, the two arrangements produce nearly identical conditional detection probabilities, so their fiber coupling efficiencies must be similar.

In order to decide which estimate is better, we must consider the uncertainties of each method. Both methods use measurements of the conditional detection probability and the insertion loss of components to isolate the fiber coupling efficiency, so these uncertainties are found in both methods. Comparing the waveguide and bulk crystals, however, allows us to eliminate the unknown losses which are also included in the 50-60% estimate found in section 4.3. The setup and detectors are experimental, so it is certainly possible that we have missed important losses. For instance, it is possible that the TAC and SCA are missing some of the detector pulses that are seen by the counter, introducing a loss in the coincidence rate. A discriminator could be used after each of the detectors to see if this affects the coincidence rate.

Another advantage of the waveguide and bulk comparison method is that it uses smaller, lower uncertainty losses. The method in section 4.3 requires us to correct for all of the losses, each of which has an uncertainty. These uncertainties add up when we are trying to determine what fraction of the ~18 dB total loss is attributable to the fiber coupling. Furthermore, measuring the insertion loss of optical components is much more accurate than measuring the detection efficiency of a photon counter. It is certainly possible that the HP 81532A power meter module is not as accurate as specified at measuring in the low picowatts. A few picowatt error would significantly change the detection efficiency numbers, so there is a large uncertainty on the estimate of fiber coupling efficiency given in section 4.3. It is important to note, however, that 69% estimate for the photon's transmission through the narrowband is not affected by the

uncertainty in the detection efficiency or any other loss. This calculation is made by comparing the conditional probabilities of detection with and without the narrowband filter, so it has the advantages we are finding for the waveguide and bulk comparison method.

There are, however, two uncertainties about the bulk and waveguide comparison method. First, the comparison was performed without a spectral filter, so any differences in fluorescence bandwidth would change the effective detection efficiency, introducing an error in the estimate. Using a spectral filter when making the comparison could eliminate this error. The second issue is whether the classical losses in the waveguide are equivalent to the losses seen by downconverted photons. It is possible that some pairs are produced such that one of the photons is guided while the other is lost into the cladding. This type of propagation loss cannot be measured classically and should be considered in any future work involving the waveguide.

It is difficult to say which measure of the fiber coupling efficiency is more accurate. Both methods, however, indicate that a good coupling efficiency was obtained. Furthermore, the experimental setup allowed a successful demonstration of the spectral quantum magic bullet effect, the main goal of this thesis. The continuous variable entanglement at the heart of the quantum magic bullet effect has been the subject of some recent attention. Continuous variable quantum teleportation [17] has been recently demonstrated experimentally [18]. There has also been theoretical work on analog quantum-error-correcting codes [19] and universal quantum computation over continuous variables [20]. Continuous variable entanglement continues to be a very active area of research and we believe this thesis confirms a small part of the entanglement picture.

## REFERENCES

---

- 1 A. Einstein, B. Podolsky, and N. Rosen, "Can quantum-mechanical description of physical reality be considered complete?," *Phys. Rev.* **47**, 777 (1935).
- 2 J. Bell, "On the Einstein Podolsky Rosen paradox," *Physics* **1**, 195 (1964).
- 3 W. Tittel, J. Brendel, H. Zbinden, and N. Gisin, "Violation of Bell's inequality by photons more than 10 km apart," *Phys. Rev. Lett.* **81**, 3563 (1998).
- 4 A. Migdall, "Correlated-photon metrology without absolute standards," *Phys. Today* **52**, 41 (1999).
- 5 A. Zeilinger, "Fundamentals of quantum information," *Phys. World* **11**, 35 (1998).
- 6 Y. Shih, A. Sergienko, M. Rubin, T. Kiess, and C. Alley, "2-photon entanglement in type-II parametric down-conversion," *Phys. Rev. A* **50**, 23 (1994).
- 7 S. Lloyd, J. Shapiro and F. Wong, "Quantum magic bullets by means of entanglement," *J. Opt. Soc. Am. B* **19**, 312 (2002).
- 8 T. Kiess, Y. Shih, A. Sergienko, and C. Alley, "Einstein-Podolsky-Rosen-Bohm experiment using pairs of light quanta produced by type-II parametric down-conversion," *Phys. Rev. Lett.* **71**, 3893 (1993).
- 9 C. Hong, Z. Ou and L. Mandel, "Measurement of subpicosecond time intervals between 2 photons by interference," *Phys. Rev. Lett.* **59**, 2044 (1987).
- 10 M. Albota, "Single-photon detection of 1.55  $\mu\text{m}$  entangled light and frequency upconversion in periodically poled lithium niobate for quantum communication," Master's Thesis, MIT (2002).
- 11 L. Myers, R. Eckardt, M. Fejer, R. Byer, W. Bosenberg, and J. Pierce, "Quasi-phase-matched optical parametric oscillators in bulk periodically poled  $\text{LiNbO}_3$ ," *J. Opt. Soc. Am. B* **12**, 2102 (1995).
- 12 P. Baldi, M. Sundheimer, K. ElHadi, M. deMicheli, and D. Ostrowsky, "Comparison between difference-frequency generation and parametric fluorescence in quasi-phase-matched lithium niobate stripe waveguides," *IEEE J. of Sel. Top. in Quantum Electron.* **2**, 385 (1996).
- 13 C. Kurtsiefer, M. Oberparleiter, and H. Weinfurter, "High-efficiency entangled photon pair collection in type II parametric fluorescence," *Phys. Rev. A* **64**, 3802 (2001).

---

14 F. Bovino, P. Varisco, A. Colla, G. Castagnoli, G. Di Giuseppe, and A. Sergienko, “Effective fiber-coupling of entangled photons for quantum communication,” quant-ph/0303126, submitted to Optics Letters (2003).

15 B. Saleh and M. Teich, Fundamentals of Photonics, John Wiley and Sons, Inc. (1991).

16 S. Tanzilli, H. De Riedmatten, W. Tittel, H. Zbinden, P. Baldi, M. De Micheli, D. Ostrowsky, and N. Gisin, “Highly efficient photon-pair source using periodically poled lithium niobate waveguide,” Electron. Lett. **37**, 26 (2001).

17 L. Vaidman, “Teleportation of quantum states,” Phys. Rev. A **49**, 1473 (1994).

18 A. Furusawa, J. L. Sørensen, S. L. Braunstein, C. A. Fuchs, H. J. Kimble, and E. S. Polzik, “Unconditional quantum teleportation,” Science **282**, 706 (1998).

19 S. L. Braunstein, “Error correction for continuous quantum variables,” Phys. Rev. Lett. **80**, 4084 (1998); S. L. Braunstein, “Quantum error correction for communication with linear optics,” Nature **394**, 47 (1998); S. Lloyd and J.-J. E. Slotine, “Analog quantum error correction,” Phys. Rev. Lett. **80**, 4088–4091 (1998).

20 S. Lloyd and S. L. Braunstein, “Quantum computation over continuous variables,” Phys. Rev. Lett. **82**, 1784 (1999).